AIMS Materials Science, 13(3): 410–443.
DOI: 10.3934/matersci.2026021
Received: 11 March 2026
Revised: 05 May 2026
Accepted: 12 May 2026
Published: 21 May 2026

https://www.aimspress.com/journal/Materials

Research article

A multiscale model for tensile response of fique fiber-reinforced composite laminates

Sergio A. Gomez-Suarez[1,2,*] and Joszaira Lárez-Natera[3,4]

[1] Faculty of Mechanical Engineering, Universidad Pontificia Bolivariana, Km 7 Autopista Vía Piedecuesta, Floridablanca, Santander 681001, Colombia
[2] Doctorate in Engineering Program, Universidad Católica Andrés Bello, Av. Teherán, Urb. Montalbán, Caracas, Distrito Capital 1020, Venezuela
[3] Department of Physics, Faculty of Engineering, Universidad Católica Andrés Bello. Av. Teherán, Urb. Montalbán, Caracas, Distrito Capital 1020, Venezuela
[4] Department of Physics, Faculty of Science, Universidad Central de Venezuela. Ciudad Universitaria de Caracas, Av. Los Ilustres, Los Chaguaramos, Caracas, Distrito Capital 1040, Venezuela

* **Correspondence:** Email: sergio.gomezs@upb.edu.co; Tel: +57-607-679-6220.

Abstract: The incorporation of natural fibers into composite materials has attracted growing interest due to their low cost, regional availability, and reduced environmental impact. However, their adoption in industrial applications remains limited by the absence of reliable predictive models linking constituent properties with the laminate's macroscopic behavior. In this context, this work developed and validated a multiscale predictive model to estimate the tensile behavior of laminates reinforced with fique fiber. The approach first evaluates classical micromechanical predictions (Chamis model) against experimentally characterized ply properties, demonstrating that idealized analytical formulations fail to capture the structural heterogeneity of twisted natural fibers. Consequently, experimentally obtained ply data were used as direct inputs for classical laminate theory (CLT) and finite element method (FEM) simulations to ensure accurate laminate-level predictions. The predictions were experimentally validated according to ASTM D3039 in [0º/90º/0º], [90º/0º/90º], and [90º/0º/45º] configurations. The results showed that the Chamis model systematically underestimates longitudinal strength and overestimates transverse stiffness due to assumptions that do not accurately represent natural fibers. In contrast, when both CLT and FEM were informed by the experimental properties of the unidirectional ply, they achieved predictions consistent with the tests: the combined coefficient of determination of 0.69 for CLT and 0.70 for FEM, with mean absolute errors of 16.65 and 16.04 MPa, respectively.

Keywords: biocomposites; finite elements; fique; laminates; multiscale modeling

1. Introduction

Growing environmental pressure and the demand to reduce the adverse effects of synthetic materials have driven the search for more sustainable composites [1]. In this scenario, natural plant fibers emerge as viable alternatives not only due to their low cost, regional abundance, and biodegradability but also because of their reduced carbon footprint and potential to replace synthetic reinforcements in a wide range of applications [2].

However, despite growing interest, the industrial implementation of natural fibers in composite materials remains limited. As noted by Mulenga et al. [3], this constraint is primarily due to the absence of reliable predictive models capable of accurately predicting their mechanical behavior. The anisotropic and heterogeneous nature of these fibers, coupled with the inherent complexity of laminates, necessitates advanced approaches that integrate laminate theories and robust computational methods. In the absence of such tools, material design relies heavily on costly experimental tests with limited generalizability, hindering property optimization and restricting their adoption in diverse applications.

Among the most studied natural fibers are hemp, sisal, jute, and kenaf [4–6]. However, the search for regional alternatives offering technical competitiveness and economic viability continues to expand. In this framework, fique fiber (Furcraea spp.), native to Latin America, has attracted growing interest due to its high holocellulose content and low lignin and pectin content, properties that enhance adhesion to polymeric matrices and confer intrinsic mechanical strength [7]. These characteristics, coupled with its abundance in countries like Colombia, where over 15,000 hectares are cultivated, generating thousands of tons of fiber and by-products annually, establish fique as a strategic candidate for biocomposite development, particularly in regions where its cultivation is widespread and sustainable, in alignment with policies transitioning toward renewable materials [8].

The literature on fique-reinforced composites primarily focuses on experimental characterization, without yet consolidating the development of multiscale predictive models. For instance, Laverde Sarmiento et al. [9] conducted chemical and mechanical characterization of treated and untreated fique fibers, evaluating stress-strain curves under tensile loading for their potential use as concrete reinforcement. Similarly, Pabón Rojas et al. [10] investigated fique/epoxy biocomposites processed via vacuum-assisted techniques, finding that fiber-matrix compatibility and vacuum level significantly influence mechanical properties. In a complementary approach, Rua et al. [11] evaluated epoxy-fique laminates using Charpy impact tests, three-point bending, and Split-Hopkinson dynamic tests. The authors demonstrated that incorporating bidirectional fique layers notably increases energy absorption and flexural strength, an effect attributed to mechanisms such as crack deflection and adequate fiber-matrix adhesion.

Consistent with this trend, the review conducted by Gómez and Córdoba [12] on fique fiber-reinforced composites reveals that most studies focus on fiber treatments, matrix selection, and manufacturing processes. In contrast, predictive approaches remain scarce and, when applied, are limited to basic approximations. While some studies have employed simple analytical models and finite element simulations to estimate global properties, they have not incorporated multiscale strategies nor considered the inherent variability of natural fibers, thereby reaffirming the gap identified in the literature.

Regarding predictive models, studies in the literature remain limited. Barros et al. [13] developed a finite element model to analyze the flexural behavior of fique composites, achieving differences of less than 6.8% between numerical and experimental results for elastic constants, but without integrating a micromechanical approach to explain behavior from the constituent level. González-Estrada et al. [14] applied homogenization models to woven fique composites, although without adequately considering the inherent variability of natural fibers. Other studies, such as Chaves et al. [15], modeled specific behaviors (fatigue) without establishing a connection to basic mechanical properties, while Avila et al. [16] used the Johnson-Cook model for ballistic analysis with parameters obtained mainly through empirical calibration and without multiscale validation.

Furthermore, Castro et al. [17] applied the finite element method to analyze a wind turbine blade manufactured with fique composites, accounting for material anisotropy and proposing a structural redesign. However, the study did not include experimental validation or predictive optimization processes, limiting the scope of its results. In a complementary study, Gómez et al. [18] conducted a comparative modal analysis of fique composites using finite element simulation and analytical modeling; however, the material was assumed to be isotropic, limiting the representation of the anisotropic behavior inherent to laminates reinforced with aligned fibers. Similarly, in a study on school furniture manufacturing, Gómez et al. [19] employed finite element simulation for structural design assessment, although again under the assumption of material isotropy.

In summary, the current literature on fique fiber-reinforced composite materials presents significant limitations, such as the absence of multiscale approaches that coherently integrate the micromechanical, ply, and structural levels; a strong reliance on empirical calibrations lacking a rigorous theoretical basis; a scarcity of systematic studies on laminates with controlled reinforcement orientations and volume fractions; and, consequently, limited predictive capability to estimate mechanical properties based on the characteristics of the material constituents.

To address these specific deficiencies, continuum-based multiscale modeling emerges as a highly promising strategy. By enabling the explicit linkage of the intrinsic properties of the constituents with the macroscopic response of the laminate, this approach reduces the need for costly experimental tests and enhances extrapolation capabilities in the rational design of composite materials [20,21].

While this continuum-based approach effectively resolves the immediate ply-level estimation gaps for biocomposites, it is also essential to situate it within the broader, rapidly advancing modeling landscape. In this wider context, the research field is increasingly integrating complementary methodologies that span from atomistic insights to rate-sensitive structural responses. At the nanoscale, molecular dynamics simulations have proven effective in elucidating interfacial bonding mechanisms and energy dissipation pathways; for instance, Zhang et al. [22] demonstrated that oriented graphene oxide coatings enhance damping capacity through interlayer slip, offering microscopic criteria that can refine constitutive assumptions at higher scales. To bridge these atomistic insights with continuum representations, hierarchical homogenization frameworks, such as the sequential multiscale approach by Shu and Stanciulescu [23], rigorously incorporate interface imperfections by coupling micromechanical formulations with mean-field methods, enabling efficient upscaling to macroscopic effective properties. At the structural level, rate-dependent damage formulations, such as the continuum framework proposed by Fedorenko et al. [24] for thin-ply CFRP under impact, illustrate how dynamic failure can be captured without resorting to computationally intensive cohesive zone models. Although these advanced methodologies exceed the quasi-static scope

of the present study, acknowledging them helps contextualize the current modeling landscape and outlines clear pathways for future research on interface-optimized or dynamically loaded biocomposites.

In this context, the present paper aims to develop and validate a hybrid multiscale predictive model to estimate the tensile behavior of laminates reinforced with fique fiber. Rather than relying solely on theoretical estimates, the proposed methodology first employs the Chamis micromechanical model as a diagnostic baseline. This step serves to quantify the systematic deviations that arise when standard continuum-based micromechanics are applied to highly anisotropic and twisted natural reinforcements. By explicitly demonstrating these limitations, the study justifies its core approach: utilizing experimentally characterized unidirectional ply properties as the reliable foundation for structural upscaling. These empirical inputs are subsequently integrated into the classical laminate theory (CLT) to estimate the global response of the laminate and further validated through finite element method (FEM) simulations and experimental tests on representative configurations ([0º/90º/0º], [90º/0º/90º], and [90º/0º/45º]).

2. Materials and methods

2.1. Materials

Twisted fique yarn in its traditional commercial form, widely available in the Colombian market, was used as reinforcement. This material consists of manually twisted fiber bundles. Unlike technically braided or woven structures, this twisted architecture does not involve multi-axial interlacing. Instead, it consists of fiber bundles helically twisted together, which allows for filament rearrangement under load. Consequently, this configuration results in a lower apparent stiffness compared to the intrinsic modulus of individual fique fibers. The average diameter of the twisted fique yarn was 1150.97 ± 8.63 µm, while the individual fibers exhibited a diameter of 213.38 ± 1.32 µm, as determined by scanning electron microscopy (SEM) performed on a Tescan MIRA3 system operated at 30 kV. Prior to analysis, the samples were sputter-coated with a gold layer using a Cressington 108 Auto sputter coater to enhance surface conductivity and improve image quality (Figure 1).

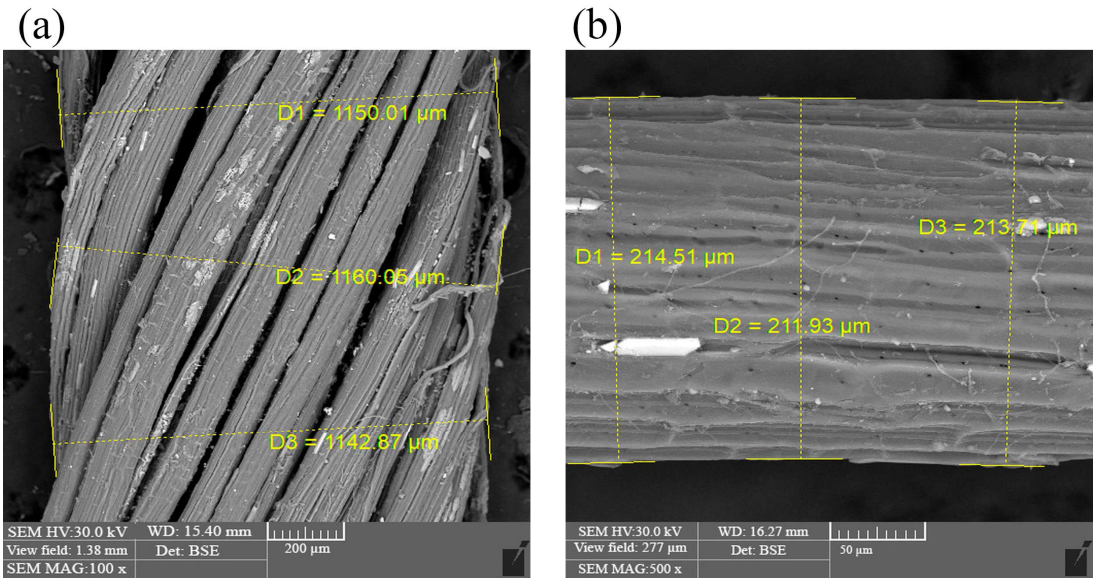

Figure 1. Morphological characterization of fique fiber: (a) twisted fique yarn; (b) individual fiber.

The matrix used was an ortho-phthalic unsaturated polyester resin, supplied by Tecnoquímicas S.A.S. (Santander, Colombia). According to the technical data sheet, this system exhibits a viscosity of 550 ± 25 mPa·s and a density of 1.25 g/cm^3 at 25 °C, conditions that facilitate adequate fiber impregnation. The solids content is 65%, with a gelation time of 18 ± 2 min at room temperature. The curing system was activated by the addition of methyl ethyl ketone peroxide (MEKP) as a curing agent at 2 wt.% relative to the resin mass, in accordance with the manufacturer's specifications.

2.2. Chemical treatment of fique fibers

To improve interfacial adhesion between the polymeric matrix and the fique fibers, an alkalization treatment was applied. The procedure consisted of immersing the fibers in a 10% w/v aqueous sodium hydroxide (NaOH) solution for 60 min at 23 ± 2 °C.

Subsequently, the fibers were neutralized through successive rinsing, first with distilled water and then with a dilute 1% v/v acetic acid solution, until a neutral pH (7.0 ± 0.2) was achieved, as verified using a digital pH meter (Hanna Instruments, model HI98107).

Drying was performed in two stages: first under ambient conditions (23 ± 2 °C and 50 ± 11% relative humidity **(**RH)) for 24 h, followed by drying in a forced convection oven (Binder, Model FD23) at 60 ± 1 °C for 8 h. This protocol allowed for the removal of residual moisture without inducing thermal degradation.

2.3. Mechanical characterization of constituent materials

The mechanical properties of the polymeric matrix and the twisted fique yarn reinforcement were evaluated using uniaxial tensile tests on an MTS C43.104 universal testing machine (10 kN capacity), following the crosshead speeds, specimen geometries, and conditioning protocols established in the corresponding standards.

The tensile properties of the polymeric matrix were evaluated in accordance with ASTM D638-22, using Type I specimens fabricated by casting with a nominal thickness of 3.2 mm (Figure 2). Curing was carried out in two stages: first, 24 h at 23 ± 2 °C, followed by post-curing at 60 °C for 8 h in a forced convection oven. The testing speed was 5 mm/min.

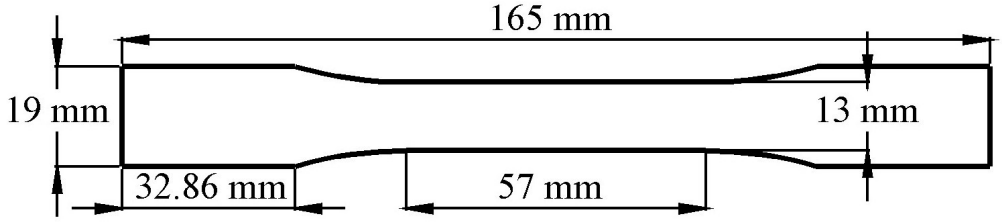

Figure 2. Polyester resin specimen geometry according to ASTM D638-22.

In-plane shear properties were evaluated in accordance with ASTM D5379/D5379M-19, using double V-notched specimens (Figure 3), cured under the same conditions as the tensile specimens. The testing speed was 2 mm/min.

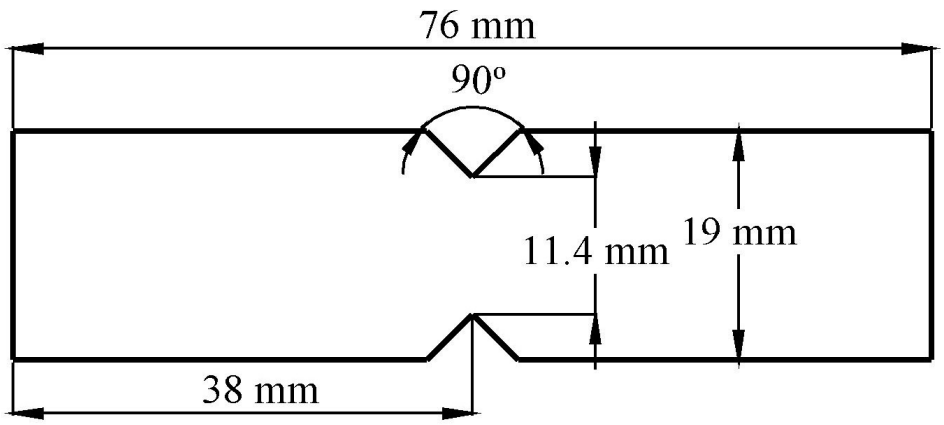

Figure 3. Polyester specimen geometry according to ASTM D5379/D5379M-19.

The compressive properties of the matrix were determined in accordance with ASTM D695-23, employing cylindrical specimens 12.7 mm in diameter and 25.4 mm in height, which were also cured following the same protocol. The testing speed was 1.3 mm/min.

The mechanical characterization of the twisted fique yarn was performed using tensile tests according to ASTM C1557-20. The samples, with a gauge length of 50 mm, were conditioned for 72 h prior to testing under controlled conditions (23 ± 2 °C and 50 ± 11% RH) to stabilize their moisture content and were tested at a speed of 0.48 mm/min.

Due to the experimental limitations inherent to natural fiber compression tests, caused primarily by the premature buckling of fibers [25], the compressive strength of the fique fiber (σ_{Cf}) was not measured directly. Instead, an empirical relationship employed for natural fibers was used, which states that compressive strength typically ranges between 0.5 and 0.8 times the tensile strength (σ_{Tf}) [26]. For the purposes of this study, the mean value of this range was adopted, as expressed in Eq 1:

$$\sigma_{\mathrm{Cf}} = 0.65\sigma_{\mathrm{Tf}} \tag{1}$$

The fique fiber was modeled as an isotropic material as a first-order approximation, allowing the shear modulus (G) to be calculated from the elastic modulus (E) and Poisson's ratio (v) using the classical relationship shown in Eq 2 [27].

$$G = \frac{E}{2(1+v)} \tag{2}$$

Figure 4 shows the experimental setups employed for mechanical characterization of the matrix and fique fiber reinforcement. For each mechanical test group—matrix tensile (ASTM D638-22), matrix shear (ASTM D5379/D5379M-19), matrix compression (ASTM D695-23), and twisted fique yarn tensile (ASTM C1557-20)—five specimens (n = 5) were tested in accordance with the minimum replicate requirement established by the respective standards for reliable property estimation. Results are reported as mean ± standard deviation to convey the inherent data dispersion observed in natural fiber systems.

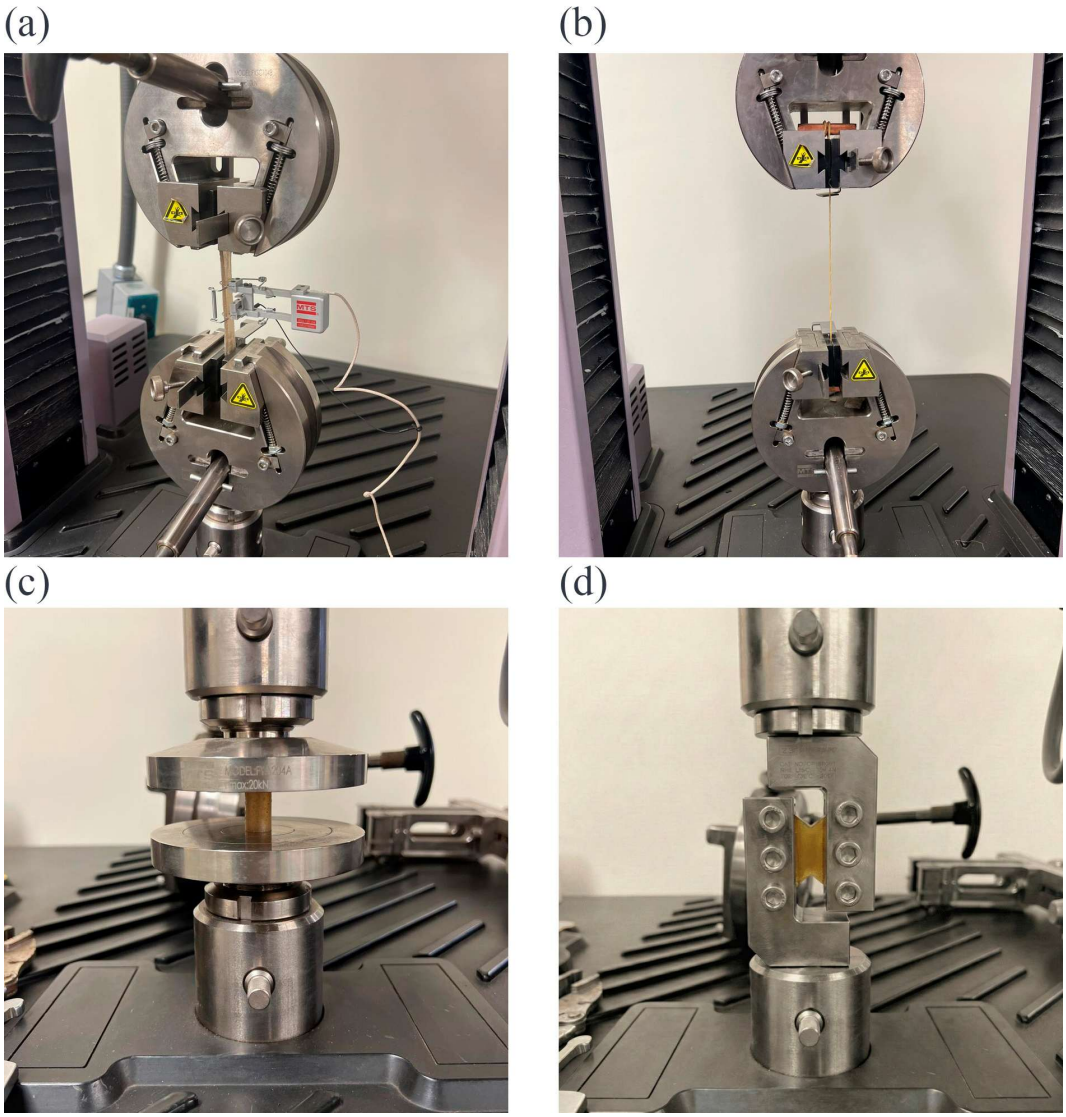

Figure 4. Experimental setups: (a) matrix tensile test; (b) twisted fique yarn tensile test; (c) matrix compression test; (d) matrix shear test.

2.4. Micromechanical modeling of the unidirectional ply using the Chamis model

For the theoretical estimation of the mechanical properties of the unidirectional ply, the micromechanical model proposed by Chamis has been widely employed in the analysis of fiber-reinforced composites. This approach allows for the prediction of both elastic and strength properties of the ply based on the characteristics of its constituents (matrix and reinforcement) and the fiber volume fraction (V_f). The model assumes a uniform distribution of continuous, aligned fibers with ideal interfacial bonding embedded within a homogeneous matrix [28,29].

In this study, the Chamis model is employed as an analytical reference to evaluate classical micromechanical predictions.

The elastic properties of the unidirectional ply in the longitudinal (1) and transverse (2) directions were calculated using the expressions provided in Eqs 3–6 based on the Chamis model [30].

$$E_1 = E_f V_f + E_m(1 - V_f) \tag{3}$$

$$E_2 = \frac{E_m}{1-\sqrt{V_f}\left(1-\frac{E_m}{E_f}\right)} \tag{4}$$

$$v_{12} = v_f V_f + v_m(1 - V_f) \tag{5}$$

$$G_{12} = \frac{G_m}{1-\sqrt{V_f}\left(1-\frac{G_m}{G_f}\right)} \tag{6}$$

where E denotes elastic modulus, v is Poisson's ratio, G represents the shear modulus, V_f fiber volume fraction and the subscripts *f* and *m* correspond to the fiber and matrix phases, respectively.

It should be noted that, given the absence of experimental data on the transverse behavior of fique fiber, the simplification of assuming that its transverse properties are equivalent to the longitudinal ones was adopted. While this approximation is common in preliminary studies on natural fibers, it does not adequately reflect their marked anisotropy. Despite this limitation, this idealization was considered acceptable for the implementation of the Chamis micromechanical model, while explicitly acknowledging that it may introduce significant errors, particularly in the prediction of the transverse modulus of the unidirectional ply.

The strength properties of the unidirectional ply were estimated from the constituent materials using empirical relationships defined by the Chamis model [31] as presented in Eqs 7–11.

$$X_T = V_f\, \sigma_{Tf} \tag{7}$$

$$Y_T = \sigma_{Tm}\left[1 - \left(\sqrt{V_f} - V_f\right)\left(1 - \frac{E_m}{E_f}\right)\right] \tag{8}$$

$$X_C = V_f\, \sigma_{Cf} \tag{9}$$

$$Y_C = \sigma_{Cm}\left[1 - \left(\sqrt{V_f} - V_f\right)\left(1 - \frac{E_m}{E_f}\right)\right] \tag{10}$$

$$S_{12} = S_m\left[1 - \left(\sqrt{V_f} - V_f\right)\left(1 - \frac{G_m}{G_f}\right)\right] \tag{11}$$

where X_T and X_C denote the longitudinal tensile and compressive strengths, respectively; Y_T and Y_c represent the transverse tensile and compressive strengths; and S_{12} is the in-plane shear strength of the unidirectional ply. Additionally, σ_{Tm}, σ_{Cm}, and S_m represent the tensile, compressive, and shear strengths of the polymer matrix, respectively.

2.5. Fabrication and experimental characterization of the unidirectional ply

The fabrication and experimental characterization of unidirectional plies were carried out to obtain representative mechanical properties for direct use in CLT and FEM simulations, while simultaneously contrasting these experimental values with Chamis model predictions to quantify systematic deviations arising from idealized micromechanics applied to twisted natural reinforcements. To this end, specimens were prepared with distinct fiber orientation configurations: 0° and 90° for tensile testing, 0° and 90° for compression testing, and the specific geometry for in-plane shear testing. These configurations enabled the independent evaluation of the longitudinal (E_1, v_{12}, X_T),

transverse (E_2, Y_T), and shear (S_{12}, G_{12}) mechanical properties, as well as the longitudinal and transverse compressive behavior (X_C, Y_C).

The unidirectional plies were manufactured by hand lay-up. The fique fibers were arranged on a flat mold previously treated with a release agent, ensuring alignment according to the required orientation. Subsequently, the polyester resin was applied manually and evenly, using a metal roller to ensure complete impregnation and minimize air bubbles. Curing was carried out in two stages: initially at room temperature for 24 h, followed by post-curing in a forced convection oven at 60 °C for 8 h, to maximize resin cross-linking and enhance the mechanical properties of the composite.

A fiber volume fraction of 5% was obtained, resulting from the constraints inherent to the hand lay-up process combined with the twisted bundle architecture, which limits fiber compaction and promotes resin-rich zones. Although this value falls below the critical threshold for effective reinforcement, it was deliberately maintained to reflect realistic conditions achievable with this manufacturing method and to establish a baseline for the multiscale model validation. This allows the framework to be assessed under controlled, reproducible conditions before extension to higher volume fraction systems. All plies exhibited an average thickness of 1.2 ± 0.09 mm. The volume fraction (V_f) was determined using Eq 12:

$$V_f = \frac{m_f/\rho_f}{(m_f/\rho_f)+(m_m/\rho_m)} \tag{12}$$

where m_f and m_m correspond to the fiber and matrix masses, respectively, and ρ_f and ρ_m represent the fiber and matrix densities.

The matrix mass was obtained indirectly from the total mass of the composite (m_c) and the fiber mass, according to Eq 13.

$$m_m = m_c - m_f \tag{13}$$

For tensile testing, specimens were fabricated with dimensions specified by the ASTM D3039/D3039M-17 standard: 250 mm in length and 15 mm in width for the 0° orientation, and 175 mm in length and 25 mm in width for the 90° orientation. Due to the manual hand lay-up fabrication and the irregular geometry of the twisted fique bundles, minor dimensional variations and edge irregularities were observed across the specimens. To ensure accurate stress calculations, the actual width and thickness of each sample were measured at three distinct locations within the gauge length using a digital caliper prior to testing. The average cross-sectional area was used for all mechanical property determinations, effectively mitigating the influence of geometric non-uniformity on the reported results. The fabricated specimens are shown in Figure 5.

Compression tests for both 0° and 90° fiber orientations were performed in accordance with ASTM D695-23 using a lateral support fixture, employing the specimen geometry indicated in Figure 6.

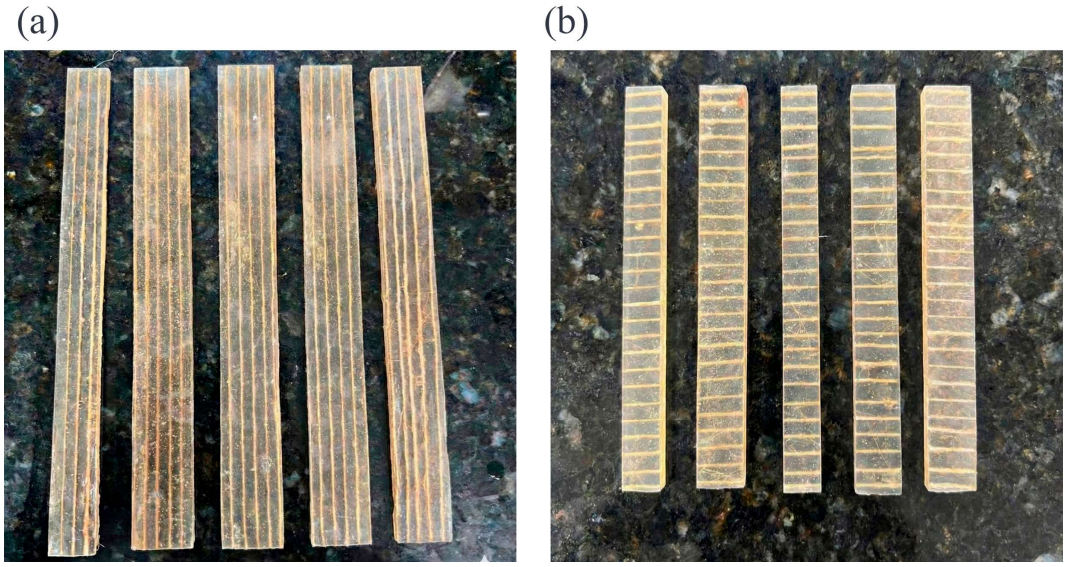

Figure 5. Ply tensile specimens: (a) 0° specimens; (b) 90° specimens.

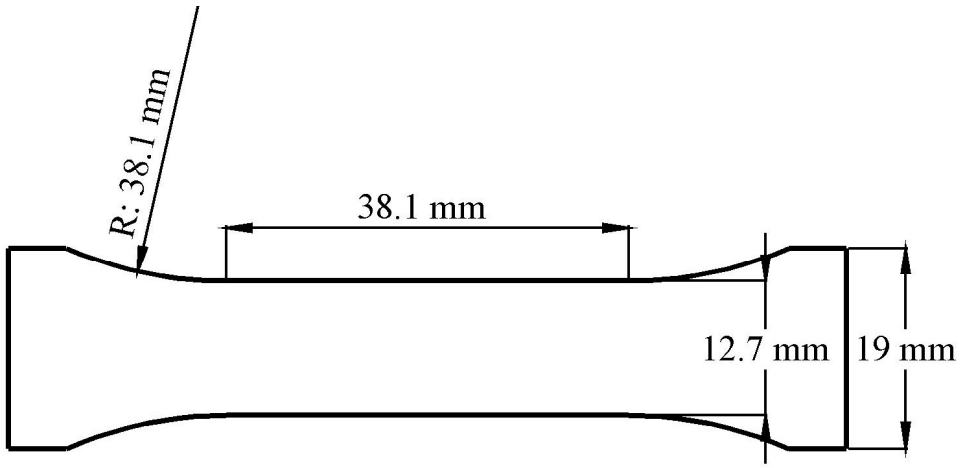

Figure 6. Laminate specimen geometry according to ASTM D695-23 standard.

For the characterization of in-plane shear behavior, specimens were fabricated with the previously mentioned double V-notch geometry, in accordance with ASTM D5379/D5379M-19.

Figure 7 shows the fabricated specimens for compression and shear characterization.

The mechanical characterization of the unidirectional plies was carried out on an MTS model C43.104 universal testing machine under controlled environmental conditions (22.8 ± 2.2 °C and 50 ± 11% RH). For each test configuration, five specimens (n = 5) were fabricated and tested: tensile tests in the longitudinal (0°) and transverse (90°) directions were performed according to ASTM D3039/D3039M-17; compression tests for both orientations followed ASTM D695-23; and in-plane shear characterization was conducted in accordance with ASTM D5379/D5379M-19. Tensile and shear tests were performed at a constant crosshead speed of 2 mm/min, while compression tests were conducted at 1.3 mm/min. Results are reported as mean ± standard deviation to reflect the inherent variability associated with the hand lay-up fabrication process.

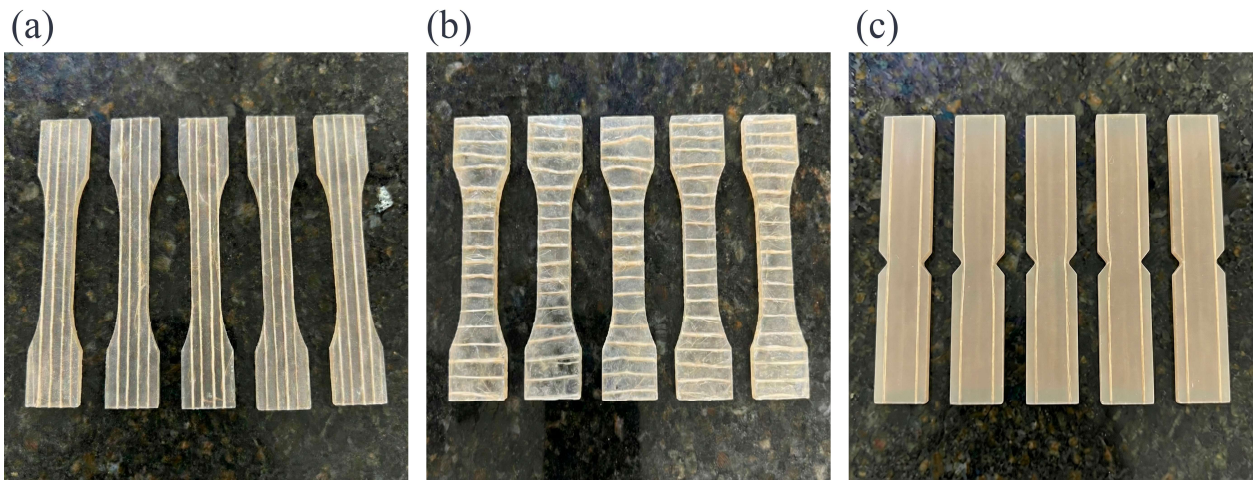

Figure 7. Ply specimens: (a) 0° specimens; (b) 90° specimens; (c) shear specimens.

2.6. Analytical modeling using CLT

The mechanical behavior of the laminates ([0º/90º/0º], [90º/0º/90º], and [90º/0º/45º]) was analyzed using an analytical approach based on CLT [32]. This model requires the engineering properties of the unidirectional ply as input, which were previously determined in preceding sections using two approaches: first, through the predictions of the Chamis micromechanical model, and second, from the experimental values obtained from the characterization of the fabricated unidirectional plies.

Based on the elastic properties $(E_1, E_2, v_{12}, G_{12})$, the reduced stiffness matrix in local coordinates (Q) was constructed for a unidirectional ply (Eq 14):

$$Q = \begin{bmatrix} Q_{11} & Q_{12} & 0 \\ Q_{12} & Q_{22} & 0 \\ 0 & 0 & Q_{66} \end{bmatrix} \tag{14}$$

where the components of this matrix are calculated using Eqs 15–18, respectively:

$$Q_{11} = \frac{E_1}{1-v_{12}v_{21}} \tag{15}$$

$$Q_{22} = \frac{E_2}{1-v_{12}v_{21}} \tag{16}$$

$$Q_{12} = \frac{v_{12}E_2}{1-v_{12}v_{21}} \tag{17}$$

$$Q_{66} = G_{12} \tag{18}$$

For each layer oriented at an angle θ_k with respect to the laminate's global coordinate system, the matrix Q was transformed using the standard transformation matrix, yielding the transformed reduced stiffness matrix, $\bar{Q}^{(k)}$.

With the $\bar{Q}^{(k)}$ matrices of all layers and their respective thicknesses, the laminate's stiffness matrix, $[ABD]$, was assembled. Its submatrices are calculated through integration across the thickness according to Eqs 19–21:

$$A = \sum_{k=1}^{n} \bar{Q}^{(k)}(z_k - z_{k-1}) \tag{19}$$

$$B = \frac{1}{2}\sum_{k=1}^{n} \bar{Q}^{(k)}({z^2}_k - {z^2}_{k-1}) \tag{20}$$

$$D = \frac{1}{3}\sum_{k=1}^{n} \bar{Q}^{(k)}({z^3}_k - {z^3}_{k-1}) \tag{21}$$

where z_k and z_{k-1} represent the upper and lower coordinates of the k-th layer with respect to the laminate's mid-plane, and n is the total number of layers in the laminate.

Given that the present study focuses on the laminate response under in-plane loading, specifically uniaxial tensile tests according to the ASTM D3039/D3039M-17 standard, bending and coupling effects were neglected. Therefore, only the extensional stiffness submatrix A was used. The relationship between the resultant mid-plane forces (N) and the mid-plane strains (ε^0), is expressed according to Eq 22:

$$\mathrm{N} = \mathrm{A}\varepsilon^0 \tag{22}$$

From this relationship, the effective longitudinal modulus of elasticity was determined for each laminate configuration using both the properties predicted by the Chamis model and those obtained experimentally.

To estimate the ultimate strength of the laminate, the Tsai-Hill failure criterion was applied analytically, layer by layer. This criterion evaluates the interaction between normal and shear stresses in the material's principal directions and is expressed as shown in Eq 23:

$$FI = \left(\frac{\sigma_1}{X}\right)^2 - \frac{\sigma_1\sigma_2}{X^2} + \left(\frac{\sigma_2}{Y}\right)^2 + \left(\frac{\tau_{12}}{S_{12}}\right)^2 \tag{23}$$

where X and Y are the tensile or compressive strengths, depending on the sign of the stress in the longitudinal and transverse directions, respectively, and S is the in-plane shear strength. The terms σ_1, σ_2, and τ_{12} represent the applied normal stress in the longitudinal direction, the normal stress in the transverse direction, and the in-plane shear stress, respectively.

Based on the mid-plane strains obtained via CLT, the local stresses in each layer were calculated for a unit axial load. These stresses were scaled proportionally until the Tsai-Hill failure index reached unity in the most critical layer. The maximum allowable nominal stress of the laminate (σ_{max}) was determined according to Eq 24:

$$\sigma_{max} = \frac{P_{\text{critical}}}{t_{\text{total}}} \tag{24}$$

where P_{critical} is the axial load per unit width corresponding to the failure state and t_{total} is the total thickness of the laminate.

2.7. Finite element simulation

Finite element modeling and analysis were performed using the SolidWorks Simulation module of the SolidWorks Research 2024 software. A virtual specimen was generated with nominal dimensions of 250 mm in length, 25 mm in width, and 3.6 mm in thickness, in accordance with the ASTM D3039/D3039M-17 standard for tensile testing of laminated composite materials. From the main face of the specimen (250 × 25 mm), a mid-surface equidistant at 0 mm was created, which was used as the analysis geometry.

Within the static analysis environment, the shell element was configured as a composite type. The laminate was defined as consisting of three layers, each 1.2 mm thick, and three stacking configurations were modeled: [0º/90º/0º], [90º/0º/90º], and [90º/0º/45º]. The mechanical properties of each layer were assigned using an orthotropic material model, with parameters obtained from both the Chamis micromechanical model and experimental values.

To correctly assign the orthotropic properties, a local coordinate system was defined on the specimen surface, aligned with its principal geometric axes. This system served as the global reference for the entire laminate. Subsequently, each layer was defined with a specific angular orientation relative to this system, allowing the material properties to be applied in the correct fiber direction.

The boundary conditions replicated those of the experimental tensile test: a fixed constraint was applied to the bottom face of the specimen (the plane defined by the width and thickness), and a uniform axial tensile load of 1000 N was applied to the opposite face in the longitudinal direction (x-axis).

The mesh was generated using the curvature-based method, with a global size of 1.58 mm, a minimum size of 0.50 mm, 8 elements per arc length, and a mesh growth ratio of 1.4. This configuration ensured adequate resolution in critical zones without compromising computational efficiency.

For the estimation of the effective modulus of elasticity, the global nominal stress of the laminate was used, calculated as the applied load (F) divided by the total cross-sectional area (A), as expressed in Eq 25:

$$\sigma_{\text{nom}} = \frac{F}{A} \tag{25}$$

This value was divided by the average strain in the loading direction (ε), obtained directly from the simulation.

The ultimate strength of the laminate (σ_{ult}) was determined using the Tsai-Hill failure criterion implemented in the software. From the simulation, the minimum factor of safety among all layers was identified, corresponding to the critical layer. The ultimate strength was calculated by multiplying the nominal stress by this minimum factor of safety (FS_{min}), as expressed in Eq 26:

$$\sigma_{\text{ult}} = \sigma_{\text{nom}} FS_{\text{min}} \tag{26}$$

In the present finite element model, the fiber–matrix interface is not explicitly discretized at the microscale. Instead, each ply is treated as a homogenized orthotropic continuum using composite shell elements, consistent with CLT. The mechanical interaction between fiber and matrix is implicitly accounted for through the effective engineering constants assigned to each layer, which were obtained either from the Chamis micromechanical model or direct experimental characterization. A perfect bonding assumption is adopted at this scale, as explicit interfacial debonding or slip mechanisms are not required for predicting the macroscopic tensile response. Global failure was evaluated using the

Tsai-Hill criterion, which operates at the ply level and inherently integrates interfacial load-transfer effects through the calibrated strength parameters

2.8. Fabrication and experimental validation of laminates

For experimental validation, composite laminate specimens were fabricated using the hand lay-up process, adhering to the nominal dimensions defined in the numerical and analytical models. The fique fiber layers were arranged sequentially in a unidirectional configuration, following the specified orientations: [0º/90º/0º], [90º/0º/90º], and [90º/0º/45º]. The [90º/0º/45º] configuration, while unconventional from a purely structural standpoint, was deliberately included to introduce in-plane shear stress components under uniaxial loading. This allows the experimental and numerical evaluation of failure mechanisms dominated by shear, specifically the activation of the Tsai-Hill criterion in the 45º oriented ply, which would not be observable in symmetric or purely orthogonal configurations. This configuration thus serves as a diagnostic tool to assess the model's predictive capability under combined stress states.

Subsequently, polyester resin was manually infiltrated onto the arranged fiber assembly, ensuring adequate wetting without significantly altering the pre-established geometry. This approach allowed for a high degree of control over fiber orientation and continuity.

The curing process was performed in the same manner as for the unidirectional plies. For each laminate configuration ([0/90/0], [90/0/90], and [90/0/45]) five specimens (n = 5) were fabricated and tested under uniaxial tension according to ASTM D3039/D3039M-17 to obtain statistically representative results. The mechanical characterization of the laminates was conducted via tensile tests on an MTS model C43.104 universal testing machine under controlled environmental conditions (22.8 ± 2.2 °C and 50 ± 11% RH), using a constant crosshead speed of 2 mm/min. Results are reported as mean ± standard deviation to reflect the inherent data dispersion associated with the hand lay-up fabrication process and natural fiber variability. The fabricated specimens are shown in Figure 8.

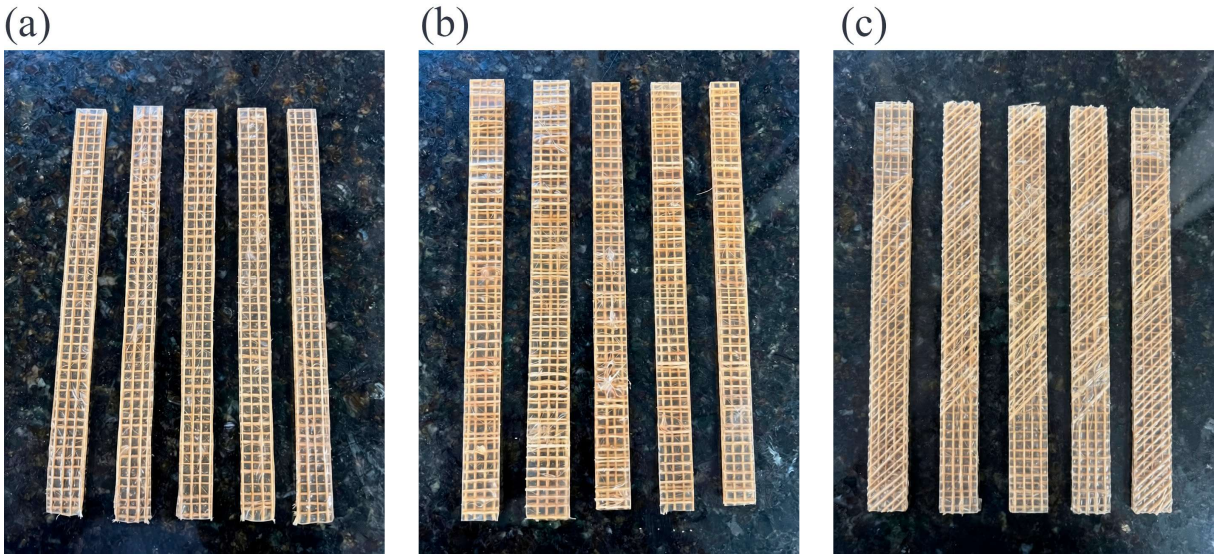

Figure 8. Fabricated laminate specimens: (a) [0º/90º/0º]; (b) [90º/0º/90º]; (c) [90º/0º/45º].

2.9. Statistical analysis

To quantitatively evaluate the predictive capability of the proposed multiscale model, a systematic comparison was performed between the experimental results obtained from tensile tests on laminates and the predictions generated by CLT and FEM simulation.

For this purpose, five complementary statistical indicators were employed: relative percentage error (RPE), mean absolute error (MAE), root mean square error (RMSE), mean absolute percentage error (MAPE), and the coefficient of determination (R^2).

The RPE was used to analyze the performance of each specific laminate configuration, allowing the identification of whether the prediction underestimates or overestimates the experimental value. It was calculated as expressed in Eq 27:

$$RPE(\%) = \frac{y^{\text{pred}} - y^{\text{exp}}}{y^{\text{exp}}} \times 100\% \tag{27}$$

where y^{pred} is the average experimental value and y^{exp} is the value estimated by the models.

The MAE and RMSE offer robust measures of the average absolute error, with RMSE being more sensitive to large errors due to its quadratic nature. Meanwhile, MAPE allows expressing the average relative error as a percentage, facilitating the comparison between variables with different magnitudes. These indicators were obtained using Eqs 28–30:

$$\text{MAE} = \frac{1}{n}\sum_{i=1}^{n}\left|{y_i}^{\text{exp}} - {y_i}^{\text{pred}}\right| \tag{28}$$

$$\text{RMSE} = \sqrt{\frac{1}{n}\sum_{i=1}^{n}({y_i}^{\text{exp}} - {y_i}^{\text{pred}})^2} \tag{29}$$

$$\text{MAPE}(\%) = \frac{1}{n}\sum_{i=1}^{n}\left|\frac{{y_i}^{\text{exp}} - {y_i}^{\text{pred}}}{{y_i}^{\text{exp}}}\right| \times 100\% \tag{30}$$

where i represents each individual observation and n is the number of observations.

These indicators were calculated both separately for the modulus of elasticity and ultimate strength, and in a combined manner, considering both variables jointly in a single output vector. This approach allows for the evaluation of the general performance of the multiscale model, while the variable-specific analysis facilitates the identification of specific deficiencies in stiffness or strength prediction.

The R^2 was used to evaluate how well the predicted values reproduce the trend of the experimental data using Eq 31:

$$\text{R}^2 = 1 - \frac{\sum_{i=1}^{n}\left({y_i}^{\text{exp}} - {y_i}^{\text{pred}}\right)^2}{\sum_{i=1}^{n}({y_i}^{\text{exp}} - \bar{y}^{\text{exp}})^2} \tag{31}$$

where $\bar{y}^{\text{exp}}$ is the mean of the experimental results. An R^2 value close to 1 indicates a high correlation between predictions and experiments, reinforcing the model's validity. Conversely, negative R^2 values indicate that the predictive model fits worse than simply using the mean of the experimental data as an estimate.

This indicator was evaluated at both the individual variable level and a global scope. However, for the global calculation, the arithmetic mean of the individual coefficients was chosen to avoid biases derived from magnitude differences between variables. This provides a comprehensive and balanced view of the model's predictive capability across all levels of analysis.

3. Results and discussion

3.1. Constituent properties

Following the 10% NaOH alkalization treatment, the diameter of the twisted fique yarn was reduced to 953.21 ± 57.73 µm, corresponding to a 17.2% decrease relative to the initial value. Concurrently, the average diameter of the individual fibers was 153.87 ± 1.45 µm, representing a 27.9% reduction. This decrease is attributed to the partial removal of hemicellulose, lignin, and pectin, which increased surface roughness and porosity, thereby promoting improved interfacial adhesion with the polymeric matrix [33] (Figure 9).

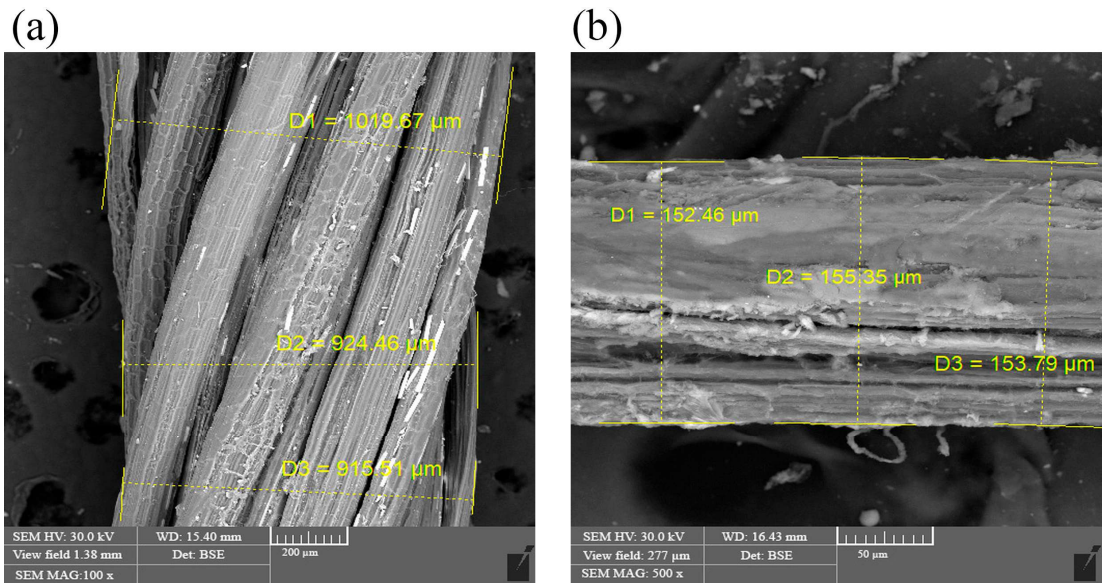

Figure 9. Morphology of alkalized fique: (a) twisted fique yarn; (b) individual fiber.

Tensile tests performed on twisted fique yarns exhibited a predominantly linear-elastic behavior up to failure, followed by a stepped rupture with distinct stress-strain curve fluctuations (Figure 10).

The tensile evaluation of the fique yarns yielded an average maximum stress of 70.06 ± 16.86 MPa and an elastic modulus of 1219.10 ± 321.20 MPa across five independent replicates tested under identical conditions. The characteristic stepped fluctuations observed in the stress–strain curves are attributable to the progressive fracture of the constituent bundles; as the helically twisted architecture rearranges under uniaxial loading, continuous load redistribution triggers localized, sequential filament failures prior to ultimate rupture. While the observed data dispersion is inherent to natural twisted reinforcements, stemming from coupled factors, such as biological heterogeneity (e.g., variations in cellulose content, microfibril angle, and intrinsic defects), the non-uniform load sharing induced by the helical geometry, and minor fabrication fluctuations (fiber alignment, resin distribution, and void content), the consistency of macroscopic trends was preserved through strict environmental

conditioning (72 h at 23 ± 2 °C and 50 ± 11% RH) and statistical averaging. Consequently, all stress–strain curves were retained for analysis, as the non-monotonic segments reflect physically meaningful failure mechanisms rather than experimental artifacts. From this representative dataset, an average Poisson's ratio of 0.38 was determined, which subsequently served as the basis for deriving the shear modulus (441.70 MPa) and compressive strength (45.54 MPa) using established empirical relationships for natural fiber systems. It should be emphasized that the reported elastic modulus corresponds to the structural stiffness of the twisted yarn assembly, not the intrinsic modulus of individual fique fibers (typically 8–9 GPa [12]); this reduced apparent stiffness arises directly from the twisted architecture, which accommodates initial deformation via filament rearrangement before engaging the full tensile load-bearing capacity of the material.

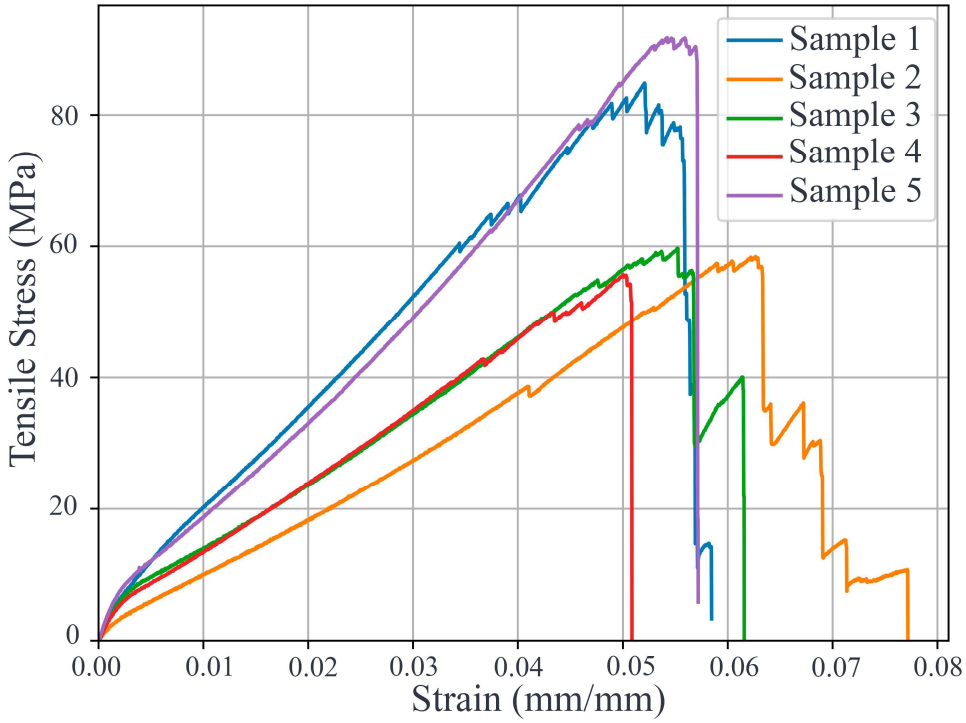

Figure 10. Stress-strain curves obtained from tensile tests for twisted fique yarn.

The polyester matrix exhibited ductile behavior with a moderate modulus of elasticity, characteristic of the specific formulation employed, which favors deformation prior to brittle fracture. The average mechanical properties were as follows: modulus of elasticity of 617.50 ± 91.20 MPa, tensile strength of 39.50 ± 5.39 MPa, and Poisson's ratio of 0.35 (Figure 11).

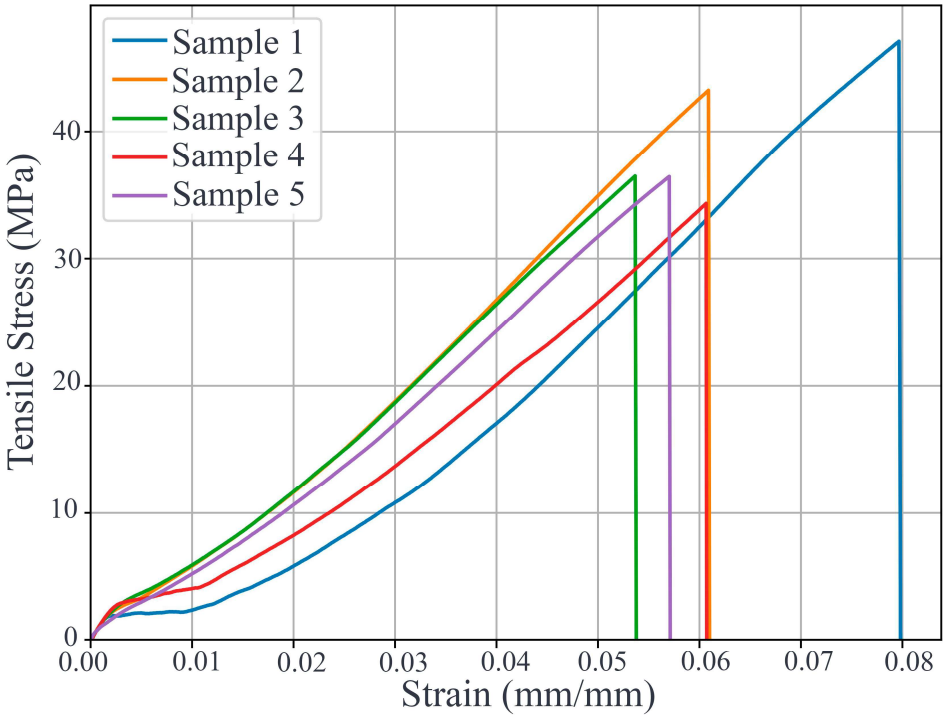

Figure 11. Stress-strain curves obtained from tensile tests for polyester.

The shear stress-strain curves presented in Figure 12 characterize the mechanical behavior of the polymeric matrix under shear loading. The average mechanical parameters obtained for the set of samples were a maximum shear stress of 10.03 ± 1.81 MPa and an average shear modulus of 209.30 ± 18.20 MPa.

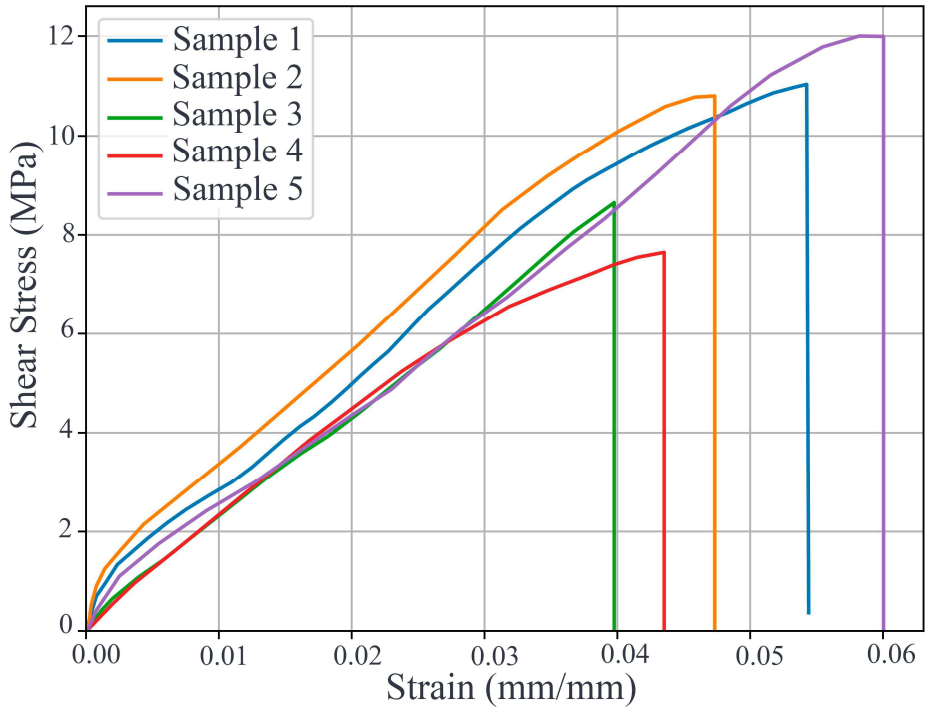

Figure 12. Shear stress-strain curves of the polymeric matrix.

Figure 13 shows the compressive stress-strain curves of the polymeric matrix. The average compressive strength was 43.10 ± 9.60 MPa, and the compressive modulus of elasticity was 1168.40 ± 187.50 MPa.

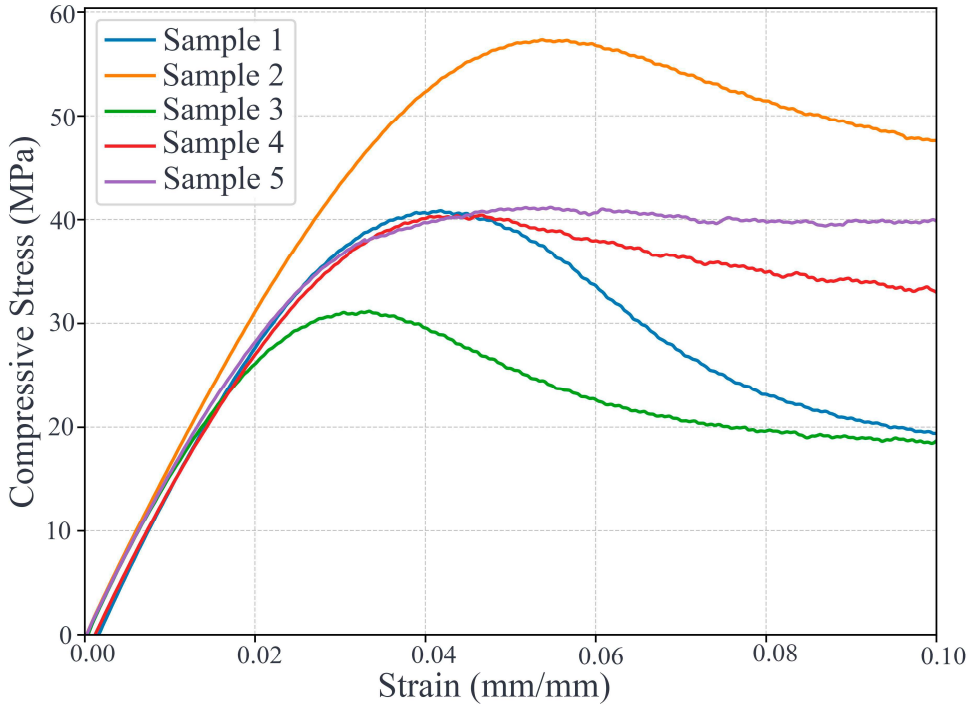

Figure 13. Compressive stress-strain curves for the polymeric matrix.

3.2. Assessment of Chamis model predictions for the unidirectional ply

Based on the constituent mechanical properties and assuming a fiber volume fraction of 5%, the Chamis micromechanical model predicted the following properties for the unidirectional ply: longitudinal (E_1 = 647.60 MPa) and transverse (E_2 = 694.10 MPa) elastic moduli, Poisson's ratio (ν_{12} = 0.35), in-plane shear modulus (G_{12} = 237.20 MPa), longitudinal (X_t = 3.50 MPa) and transverse (Y_t = 36.12 MPa) tensile strengths, shear strength (S_{12} = 9.11 MPa) and longitudinal (X_c = 2.28 MPa) and transverse (Y_c = 39.41 MPa) compressive strengths.

Experimental tensile tests on unidirectional plies with fibers oriented at 0° reported an average modulus of elasticity of 464.10 ± 77.30 MPa (coefficient of variation, CV = 16.7%), a tensile strength of 27.71 ± 3.70 MPa (CV = 13.4%), and a Poisson's ratio of 0.37 (Figure 14). The data dispersion observed in these results is a direct consequence of the intrinsic variability and structural fluctuations of the twisted fique yarn previously discussed. All stress-strain curves were retained for analysis, as non-monotonic segments corresponded to physically meaningful mechanisms, such as progressive bundle fracture and interfacial debonding, rather than experimental anomalies.

A comparison with the pure polyester matrix reveals a reduction in mechanical properties. This behavior is attributed to the low volume fraction employed. In this regime, rather than acting as the primary load-bearing element, the twisted fiber bundles introduce structural discontinuities that serve as stress concentrators within the continuous matrix [34,35].

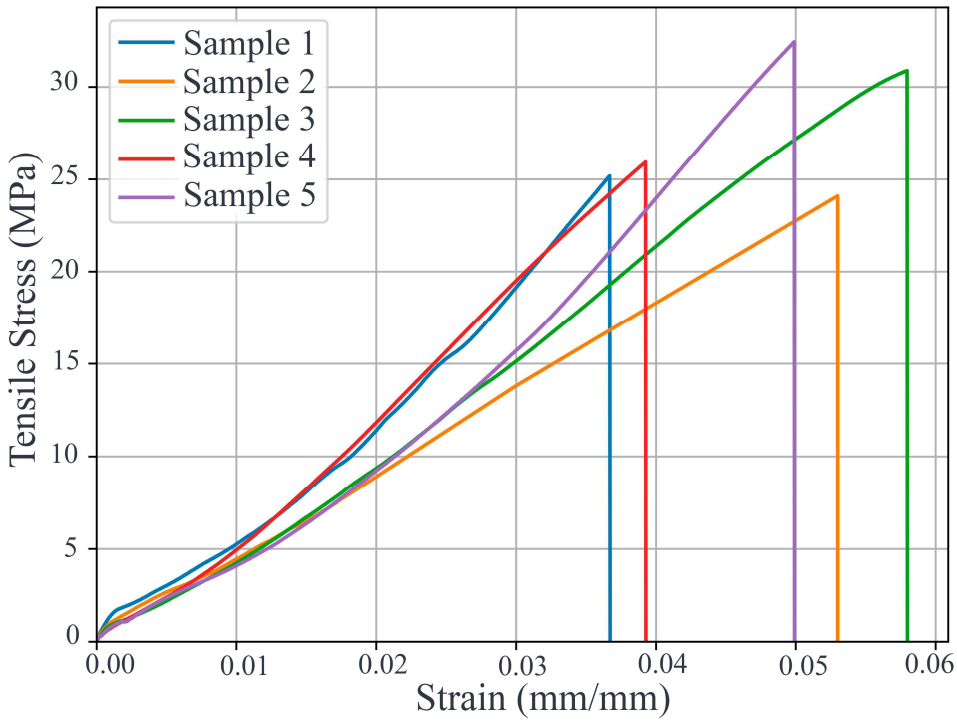

Figure 14. Tensile response of the unidirectional ply with fibers oriented at 0° (longitudinal direction).

Despite the reduction in properties relative to the pure matrix, the results obtained are comparable to those reported by Rodríguez et al. [36] for polyester composites reinforced with untreated fique, where, with a fiber mass fraction of 14.9%, a tensile strength of 18.3 MPa was achieved. It is important to highlight that, in that study, the fique fibers were not subjected to alkalization treatment or surface modification, which likely limited their adhesion to the matrix and, consequently, their efficiency as reinforcement. In contrast, the value of 27.71 MPa obtained in this work suggests that, even in a subcritical fiber fraction regime, the alkaline treatment applied to the twisted fique yarn significantly improved the fiber-matrix interface, partially mitigating the negative effects associated with the discontinuous geometry of the reinforcement.

The plies with fibers oriented at 90°, where the load is primarily supported by the matrix, exhibited a modulus of 258.80 ± 32.4 MPa and a strength of 12.92 ± 3.17 MPa (Figure 15).

The results obtained confirm the anisotropic behavior of the ply material. The 0° configuration exhibits significantly higher strength compared to the 90° orientation. This difference is explained by the fact that, under transverse loading (90°), strength depends exclusively on interfacial adhesion and matrix strength, with the fibers acting as discontinuities that facilitate crack propagation; whereas, in the longitudinal direction (0°), the matrix retains its structural continuity to support the axial load, despite operating in a subcritical fiber fraction regime [37].

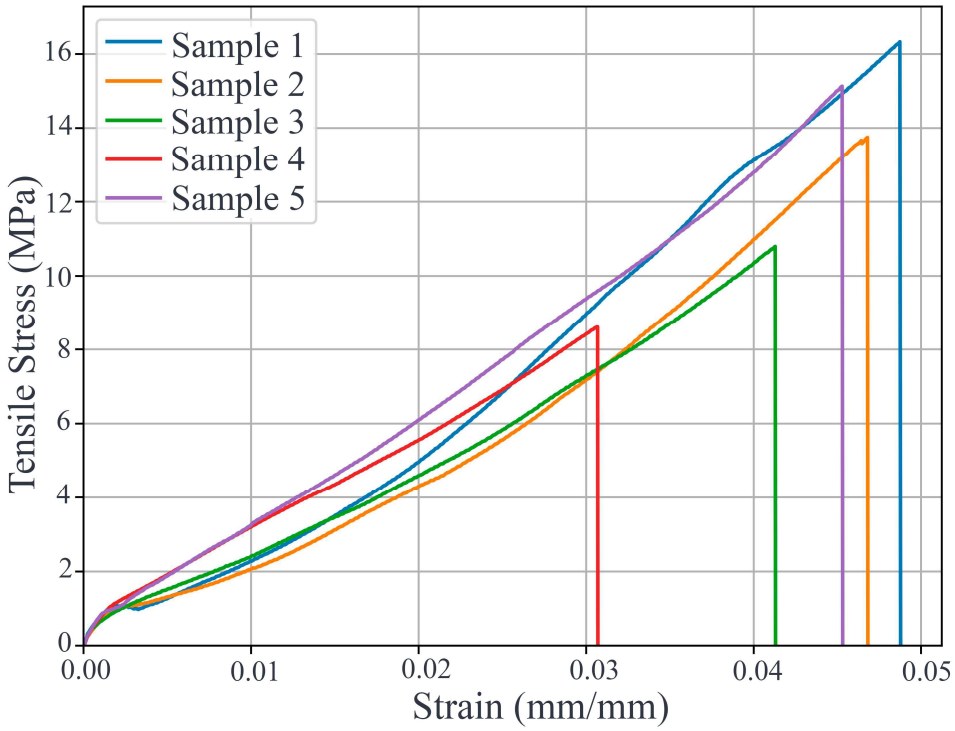

Figure 15. Tensile response of the unidirectional ply with fibers oriented at 90° (transverse direction).

The specimens subjected to shear loading exhibited an average maximum stress of 9.18 ± 0.61 MPa and an average shear modulus of 237.60 ± 17.9 MPa (Figure 16).

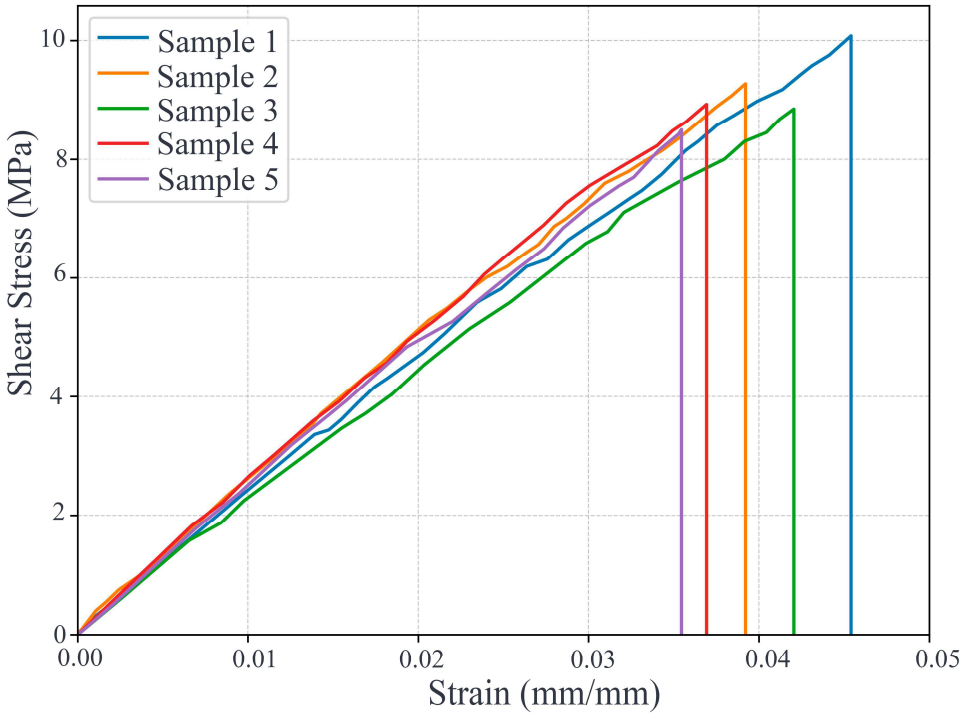

Figure 16. In-plane shear response of the unidirectional ply.

Compressive tests on unidirectional plies with fibers oriented at 0° reported an average modulus of elasticity of 1606.6 ± 481.7 MPa and a compressive strength of 50.0 ± 5.2 MPa (Figure 17).

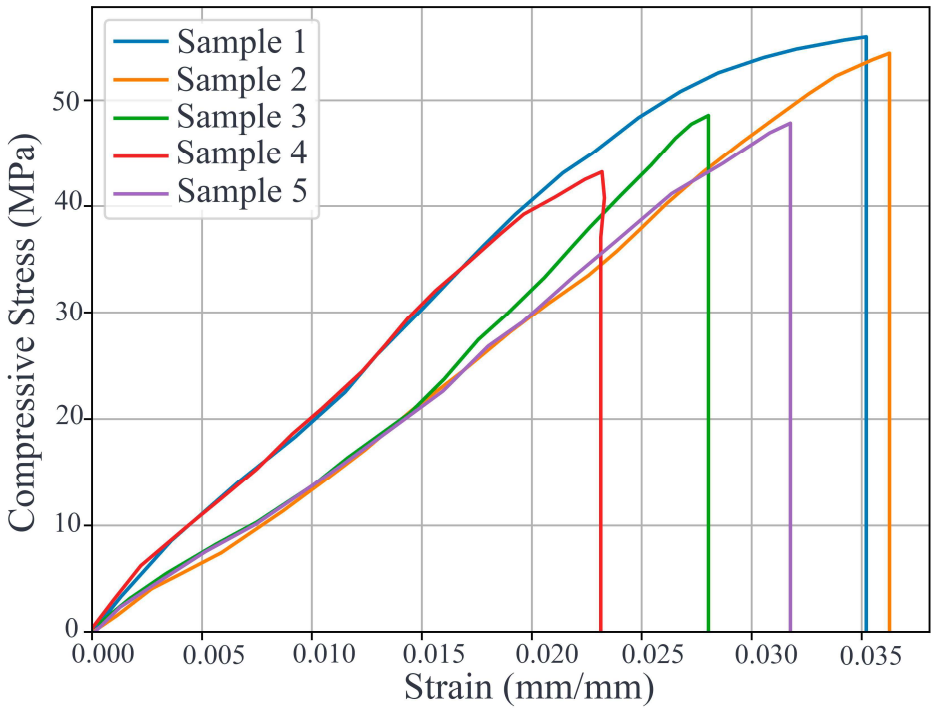

Figure 17. Compressive response of the unidirectional ply with fibers oriented at 0°.

Meanwhile, compressive tests on unidirectional plies with fibers oriented at 90° reported an average modulus of elasticity of 1423.0 ± 104.9 MPa and a compressive strength of 42.7 ± 8.4 MPa (Figure 18).

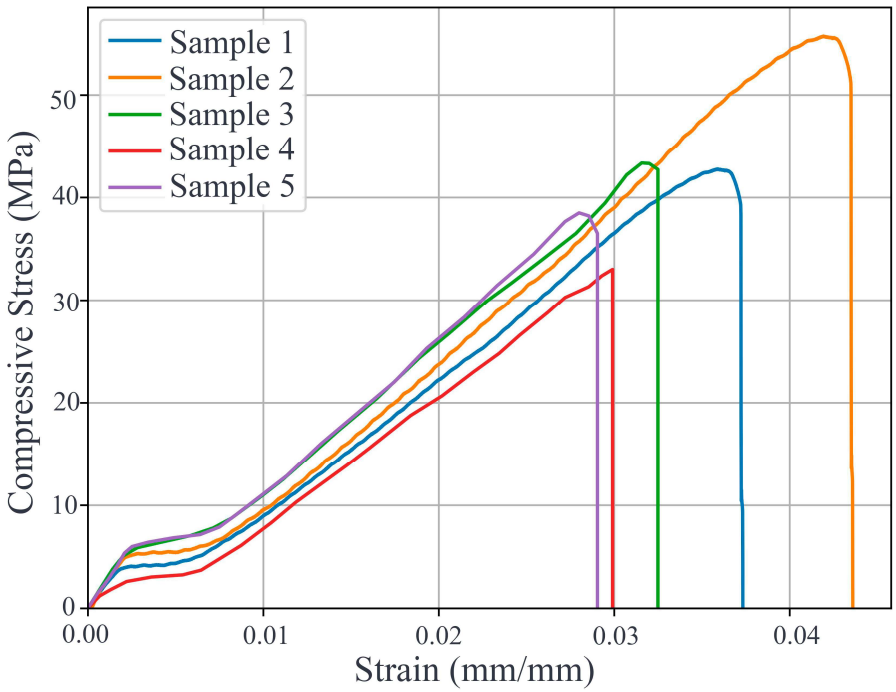

Figure 18. Compressive response of the unidirectional ply with fibers oriented at 90°.

The quantitative comparison between the model predictions and the experimental results is summarized in Table 1, which includes the RPE for each property.

Table 1. Comparison between properties predicted by the Chamis model and experimental values for the unidirectional ply.

Property	Chamis (theoretical)	Experimental	RPE (%)
E_1 (MPa)	647.60	464.10	39.54
E_2 (MPa)	694.10	258.80	168.20
G_{12}	237.20	237.60	–0.17
v_{12}	0.35	0.37	–4.86
X_T (MPa)	3.50	27.71	–87.37
Y_T (MPa)	36.12	12.92	179.57
X_C (MPa)	2.28	50.00	–95.44
Y_C (MPa)	39.41	42.66	–7.63
S_{12} (MPa)	9.11	9.18	–0.76

The Chamis micromechanical model exhibited significant limitations in predicting the properties of the unidirectional ply reinforced with twisted fique yarn. Of note is a marked overestimation of stiffness, especially in the transverse direction, where the theoretical value exceeds the experimental result by 168%. This discrepancy stems from the model's inability to differentiate between the intrinsic stiffness of the individual fiber and the effective stiffness of the twisted reinforcement. By assuming cylindrical, continuous, and perfectly aligned fibers, the approach presumes an ideal load transfer that the helical and discontinuous architecture of the actual fique cannot support [29].

Regarding strength, the deficiencies are even more pronounced. The prediction drastically underestimates the longitudinal tensile and compressive strengths relative to the experimental data, while significantly overestimating the transverse tensile strength. These extremes reflect that the Chamis equations do not capture the complex damage mechanisms inherent in natural reinforcements, such as inter-bundle delamination, fiber-matrix debonding, and stress concentrations at the fiber twist angles. Although the original Chamis model was conceived as a semi-empirical formulation, its extension to strength prediction has shown significant deviations when compared to finite element-based simulations or experimental tests [31].

Nevertheless, the model exhibits remarkable accuracy in estimating properties governed primarily by shear response and global volume fraction. Both shear modulus and shear strength present errors below 1%, and Poisson's ratio falls within acceptable margins. This result suggests that, for properties less sensitive to local fiber geometry and more dependent on the global phase proportion, the Chamis approach retains limited but significant predictive utility. This behavior is consistent with previous findings; as Habbar et al. [30] observed that the Chamis model predicts the shear modulus in reinforced materials with high fidelity, even in cases where it clearly underestimates or overestimates the transverse elastic modulus.

The major deviations are explained by the model's structural idealizations. The absence of experimental data on the transverse behavior of the fique fiber necessitated the assumption of isotropy in its properties, a simplification incompatible with the intrinsic anisotropy of vegetable fibers. Added to this approximation are further assumptions: continuity, uniform circular cross-section, and

rectilinear alignment, all of which contrast with the irregular, heterogeneous, and bundled morphology of twisted fique yarn.

The systematic discrepancies observed underscore the limitations of continuum-based micromechanical formulations when applied to twisted natural reinforcements, whose structural heterogeneity and load-redistribution mechanisms diverge from idealized continuous and aligned fiber assumptions. Consequently, the analytical and numerical predictions developed in this study were based directly on the experimentally characterized ply properties. By employing these empirical values as inputs for CLT and FEM simulations, the propagation of biases inherent to idealized micromechanical homogenization was avoided, ensuring that laminate-level estimates accurately reflect the actual structural response of the composite.

Given these observations, the applicable boundary of the Chamis micromechanical model for natural fiber-reinforced composites is largely confined to predicting properties dominated by global phase proportions and shear response, where it maintains high accuracy. The model becomes fundamentally inadequate for transverse stiffness and longitudinal strength, as its foundational assumptions (continuous, perfectly aligned, and cylindrical fibers) fail to capture the inter-bundle delamination, fiber-matrix debonding, and stress concentrations inherent to the twisted architecture of natural fique. To overcome these limitations, more precise analytical frameworks that account for fiber aspect ratios and non-ideal geometries (e.g., modified Mori-Tanaka and empirical Halpin-Tsai formulations [38]) should be considered. Ultimately, replacing idealized analytical equations with micro-scale representative volume elements (RVEs) [39] that explicitly resolve the twisted bundle morphology and incorporate cohesive zone formulations for interfacial damage represents the most robust pathway for future modeling.

3.3. Results on laminates

3.3.1. Experimental behavior

The average mechanical response obtained from the tensile tests performed on the fique fiber-reinforced laminates is presented in Figures 19 and 20, which illustrate the ultimate tensile strength and the modulus of elasticity, respectively. For each laminate configuration ([0º/90º/0º], [90º/0º/90º], and [90º/0º/45º]), five specimens (n = 5) were tested, and results are reported as mean ± standard deviation, as indicated by the error bars in both figures. The noticeable data dispersion observed at the laminate level confirms that the inherent biological variability and structural heterogeneity of the twisted fique yarn propagate from the micromechanical scale to the macroscopic composite response. This scatter originates from the combined effects of fiber-level heterogeneity, the helical bundle architecture that promotes uneven load redistribution, and minor fabrication-induced fluctuations in fiber alignment and resin distribution. Despite this inherent variability, the repeatability of macroscopic trends was preserved through strict environmental conditioning and a consistent hand lay-up protocol. Consequently, all stress–strain curves were retained for analysis, as the non-monotonic segments reflect physically meaningful failure mechanisms rather than experimental artifacts.

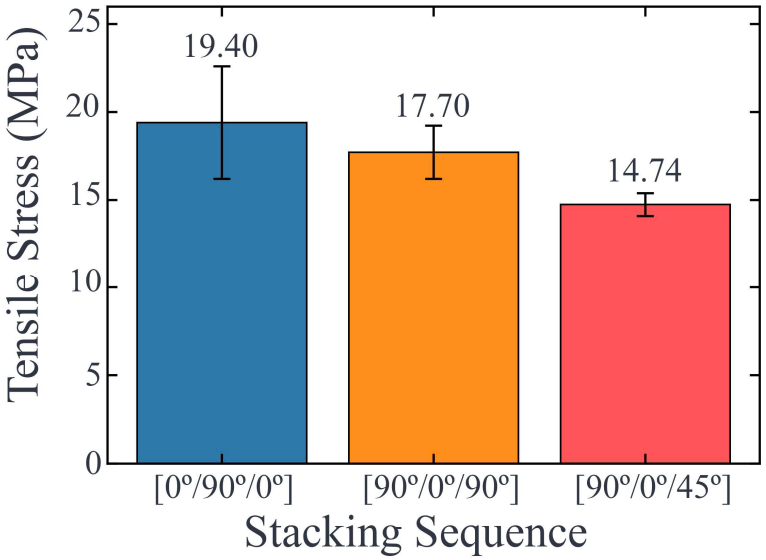

Figure 19. Experimental tensile strength of laminates.

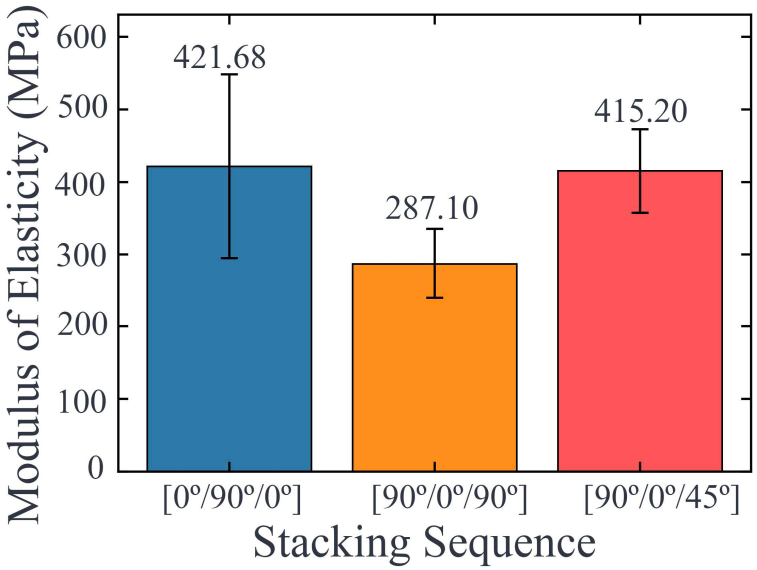

Figure 20. Experimental modulus of elasticity of laminates.

Regarding mechanical strength, the absolute values obtained demonstrate that the [0º/90º/0º] configuration exhibited superior performance, reaching an average maximum stress of 19.40 ± 3.19 MPa. This was followed by the [90º/0º/90º] arrangement with 17.70 ± 1.51 MPa, and finally the [90º/0º/45º] laminate with 14.74 ± 0.65 MPa. This variation demonstrates the strong dependence of mechanical properties on laminate architecture. The superiority of the [0º/90º/0º] arrangement is attributed to the fact that two of its three layers are aligned with the loading direction (0°), maximizing the efficiency of fiber-matrix stress transfer. In contrast, for the [90º/0º/90º] laminate, the response is dominated by the transverse layers, whose strength relies primarily on the polymeric matrix and the interface, resulting in significantly lower values.

Additionally, the [90º/0º/45º] configuration exhibited the lowest tensile strength, primarily attributable to the shear stresses induced in the 45°-oriented layer. Under axial loading, this orientation generates significant shear stress components, compromising the laminate's structural efficiency and

promoting the onset of premature interlaminar failure mechanisms, such as interlayer sliding. This behavior is widely recognized in the literature on composite materials. For instance, Ramam and Padal [40] reported that in composites reinforced with natural flax, hemp, and kenaf fibers, tensile strength in the 45° orientation decreased by 9% to 13% compared to the optimal 0° orientation, accompanied by drastically reduced elongation at break—a clear indication of premature brittle failure.

Regarding stiffness (modulus of elasticity), a similar trend was observed, although with a reversal in the order between the [90º/0º/90º] and [90º/0º/45º] configurations. The [0º/90º/0º] laminate recorded the highest stiffness (421.68 ± 126.82 MPa), followed by the [90º/0º/45º] (415.20 ± 57.60 MPa), and finally the [90º/0º/90º] (287.10 ± 48.20 MPa). These results confirm that the presence of longitudinally oriented fibers is crucial for restricting axial deformation, as also observed by Hossain et al. [41], in carbon fiber composites, where the modulus of elasticity reached its maximum at 0° and dropped to minimum values at 90°.

The notable difference in stiffness between [90º/0º/90º] and [90º/0º/45º] suggests that, although both configurations have only one layer in the loading direction, the 45° orientation introduces normal stress components that contribute to a higher global stiffness compared to purely transverse layers. This phenomenon is explained by laminate theory: 45° layers possess coupled stiffness terms that, while not maximizing axial stiffness, do enhance the global response to complex deformations [42]. In contrast, configurations with 90° layers lack this contribution, being limited by the low stiffness of the matrix.

Despite a low fiber volume fraction, the stacking architecture proved to be the governing factor in the design, where the symmetric [0º/90º/0º] configuration offers the optimal balance for axial loading applications, combining maximum strength and stiffness.

Regarding macroscopic failure modes, the laminates exhibited progressive rather than catastrophic fracture. Initial damage manifested as transverse matrix cracking, consistent with the non-linear deviations and stepped fluctuations observed in the stress–strain curves. As loading progressed, this evolved into localized fiber–matrix debonding and inter-bundle separation, driven by the twisted architecture of the fique yarns. Ultimate failure was characterized by fiber pull-out and rupture of the longitudinally aligned (0°) bundles. In configurations containing 45° and 90° plies, edge delamination and matrix-dominated shear fractures were visually evident, corroborating the stress-state predictions from laminate theory.

3.3.2. Analytical prediction via CLT

The predictive capability of CLT to characterize the mechanical behavior of fique fiber-reinforced laminates critically depends on the quality of the input properties used to describe the unidirectional ply [43]. When incorporating the theoretical elastic constants derived from the Chamis model, a marked discrepancy was observed between the predictions and the experimental results. Specifically, the theoretical approach underestimated tensile strength by approximately 81% and overestimated elastic stiffness by over 130%. These deviations reflect the inadequacy of the Chamis model's hypotheses of transverse isotropy and perfect geometry in capturing the inherent heterogeneity of natural fibers. Given that CLT directly propagates errors from the micromechanical level to the laminate analysis, such inaccuracies severely compromise its predictive utility when based on idealized parameters [44].

In contrast, the hybrid strategy employing the mechanical properties obtained experimentally for the unidirectional ply achieved high convergence with the empirical data, drastically reducing the RPE. By utilizing these experimentally characterized properties as model inputs, the multiscale framework inherently accounts for the large data dispersion characteristic of natural fibers, effectively propagating the real physical scatter that idealized micromechanical equations fail to capture. This improvement is clearly evidenced in Table 2, where the RPE values for modulus and strength fall below ±10% for all evaluated laminate configurations. These results confirm that, while CLT is sensitive to input properties, it can constitute a reliable tool for biocomposite design, provided it is supported by a representative experimental characterization that captures the material's inherent variability.

Table 2. Properties predicted via CLT using Chamis and experimental properties.

Configuration	Approach	Modulus (MPa)	Strength (MPa)	P critical (N/mm)	RPE (%) modulus	RPE (%) strength
[0º/90º/0º]	CLT-Chamis	663.2	3.58	12.896	57.28	–81.55
[0º/90º/0º]	CLT-Experimental	398.0	20.41	73.485	–5.62	5.21
[90º/0º/90º]	CLT-Chamis	678.7	3.66	13.178	136.40	–79.32
[90º/0º/90º]	CLT-Experimental	329.2	16.61	59.778	14.66	–6.16
[90º/0º/45º]	CLT-Chamis	665.0	3.59	12.911	60.18	–75.64
[90º/0º/45º]	CLT-Experimental	384.4	13.52	48.663	–7.42	–8.28

Statistical validation reinforces this analysis (Table 3). The use of theoretical properties leads to a global MAPE of 81.73% and a negative coefficient of determination (–36.60), demonstrating the invalidity of idealized micromechanical assumptions in the context of natural fibers. In contrast, when employing experimental properties, the global MAPE decreases to 7.89% with a MAE of 16.65, and the R^2 rises to 0.69, demonstrating a notable improvement in the model's predictive capability.

Table 3. Statistical performance indicators of the CLT model.

Input approach	Evaluated variable	MAE (MPa)	RMSE (MPa)	MAPE (%)	R^2
Chamis properties	Modulus of elasticity	294.32	302.27	84.62	–22.8
	Ultimate strength	13.67	13.80	78.84	–50.40
	Global (combined)	154	213.96	81.73	–36.60
Experimental properties	Modulus of elasticity	32.19	33.07	9.23	0.72
	Ultimate strength	1.11	1.11	6.55	0.67
	Global (combined)	16.65	23.40	7.89	0.69

3.3.3. Finite element simulations

The simulations performed using the FEM in SolidWorks Simulation showed that, like the analytical approach based on CLT, the predictive capability of the multiscale model is strongly conditioned by the quality of the constitutive properties used as input. When the properties estimated by the Chamis micromechanical model were employed, the FEM systematically reproduced the same errors observed in the CLT. An overestimation of the modulus of elasticity and a marked

underestimation of ultimate strength was observed, as detailed in Table 4. This consistency between both approaches reinforces the idea that the main limitation stems not from the analysis methodology, but from the low representativeness of the idealized properties of the Chamis model when applied to natural fibers with high structural heterogeneity.

Table 4. Properties predicted via FEM using Chamis and experimental properties.

Configuration	Approach	Strain (mm/mm)	FS_{Min}	Modulus (MPa)	Strength (MPa)	RPE (%) modulus	RPE (%) strength
[0º/90º/0º]	FEM-Chamis	0.01675	0.3224	663.3	3.58	57.30	–81.53
[0º/90º/0º]	FEM-Experimental	0.02792	1.84	398.0	20.44	–5.62	5.36
[90º/0º/90º]	FEM-Chamis	0.01637	0.3294	678.7	3.66	136.4	–79.32
[90º/0º/90º]	FEM-Experimental	0.03375	1.497	329.2	16.633	14.66	–6.03
[90º/0º/45º]	FEM-Chamis	0.01692	0.3186	656.7	3.54	58.16	–75.98
[90º/0º/45º]	FEM-Experimental	0.02512	1.215	442.3	13.5	6.53	–8.41

In contrast, when using the experimental properties obtained directly from the unidirectional fique fiber ply as input, the numerical model successfully reproduced both the stiffness and strength of the tested laminates with a good approximation. Furthermore, it adequately captured the relative trend among the different angular configurations, which supports the utility of FEM for comparing laminar architectures under axial loading.

Another advantage of the finite element analysis was its ability to visually identify the critical layer based on safety factors. As observed in Figure 21, in the configurations fed with experimental data for [0º/90º/0º] and [90º/0º/90º], the layers oriented at 90° showed the lowest safety factors, while in the [90º/0º/45º] configuration, the 45° layer proved to be the most vulnerable. This capability to localize risk zones within the laminate underscores the utility of FEM as a detailed structural diagnostic tool.

This layer-by-layer safety factor evaluation effectively serves as a first-ply failure (FPF) mode analysis. The Tsai-Hill criterion indicates that failure initiation is strongly mode-dependent: in the [0º/90º/0º] and [90º/0º/90º] laminates, the critical failure mode is transverse matrix cracking in the 90° plies, governed by normal stresses perpendicular to the fiber direction. Conversely, the [90º/0º/45º] configuration exhibits a shear-driven failure mode in the 45° ply. This numerical FPF prediction aligns closely with the progressive damage sequence observed experimentally, where matrix cracking and shear-induced sliding preceded ultimate fiber rupture. While the present macroscopic model does not simulate post-initiation damage propagation, the FPF analysis successfully identifies the governing failure mechanism for each architecture.

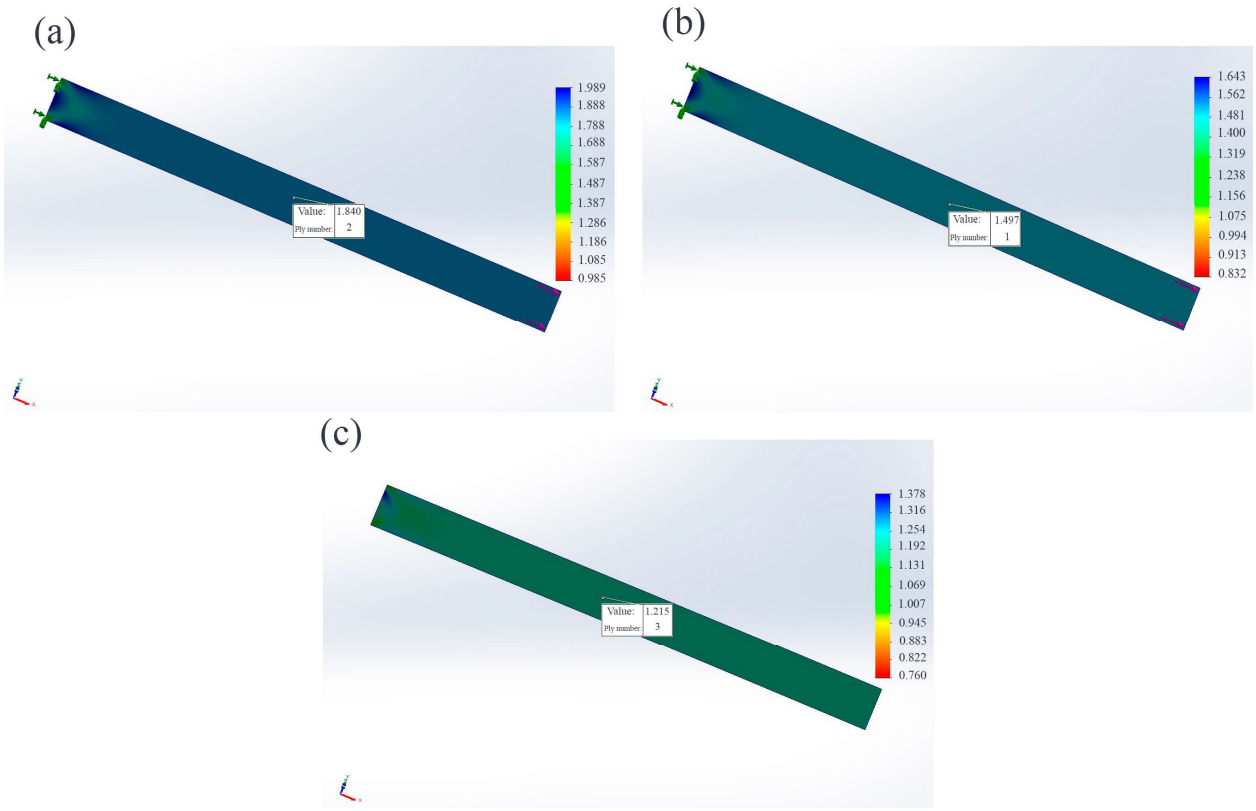

Figure 21. Critical layer and safety factor with experimental data: (a) [0º/90º/0º]; (b) [90º/0º/90º]; (c) [90º/0º/45º].

From a statistical perspective, the performance indicators presented in Table 5 show a significant improvement when experimental properties are employed. The global MAPE decreases from 81.45% to 7.77%, while the MAE is reduced from 152.6 to 16.04 MPa. The global coefficient of determination reaches a value of 0.70, indicating a strong correlation between the numerical predictions and the experimental data.

Table 5. Statistical performance indicators of the FEM.

Input approach	Evaluated variable	MAE (MPa)	RMSE (MPa)	MAPE (%)	R^2
Chamis properties	Modulus of elasticity	291.57	300.03	83.95	–22.4
	Ultimate strength	13.68	13.82	78.95	–50.50
	Global (combined)	152.6	212.34	81.45	–36.47
Experimental properties	Modulus of elasticity	30.97	31.98	8.94	0.73
	Ultimate strength	1.12	1.12	6.60	0.66
	Global (combined)	16.04	22.63	7.77	0.70

These results show that finite element modeling, when based on a rigorous experimental characterization, constitutes a solid predictive tool for laminar biocomposites. Likewise, it offers additional advantages over the analytical approach, such as the possibility of visualizing local stress,

strain, and safety factor fields, which enriches the analysis of structural behavior and facilitates the interpretation of failure mechanisms [45].

4. Conclusions

This study demonstrates that while idealized micromechanical models like Chamis serve as useful diagnostic baselines to highlight the limitations of continuum assumptions for natural fibers, their direct application leads to significant prediction errors. The proposed hybrid framework overcomes this by integrating experimentally characterized ply properties into CLT and FEM, yielding accurate tensile predictions (combined $R^2 \approx 0.70$, MAE ≈ 16 MPa), correctly capturing architecture-dependent failure modes, and identifying the [0º/90º/0º] configuration as the most structurally efficient under axial loading.

Despite its predictive success, this study presents certain limitations. Primarily, the composite laminates were restricted to a low fiber volume fraction (5%) due to the constraints of the hand lay-up manufacturing process. In this subcritical regime, the twisted fique yarns acted more as structural discontinuities than as effective reinforcement, resulting in mechanical properties that are not yet representative of high-performance structural applications.

Future research must address these limitations by validating the multiscale framework at industrially relevant fiber volume fractions (25–35%) using advanced manufacturing techniques such as vacuum-assisted resin infusion (VARI) or resin transfer molding (RTM). Additionally, to overcome the inherent micromechanical limitations identified in this work, future studies should incorporate geometry-aware analytical frameworks (e.g., modified Halpin-Tsai and Mori-Tanaka formulations) alongside the construction of thermo-mechanical constitutive models to evaluate temperature- and rate-dependent performance, as well as the explicit modeling of multi-scale interface failure mechanisms, such as cohesive zone formulations or micro-scale representative volume elements, to deeply understand fiber-matrix debonding, inter-bundle delamination, and progressive damage propagation in natural fiber composites.

Use of AI tools declaration

The authors declare that they have used Artificial Intelligence (AI) tools in the creation of this article. Specifically, Google's Gemini was utilized throughout the entire manuscript to translate the original text from Spanish to English, refine sentence structures, and improve the overall readability and flow of the paragraphs. Following the journal's guidelines, the authors conducted a rigorous human review of all AI-translated and refined text to ensure scientific accuracy, validate the appropriate academic tone, and verify that the core research data remains unaltered and strictly original.

Acknowledgments

The authors gratefully acknowledge the support provided by Universidad Pontificia Bolivariana and Universidad Católica Andrés Bello for the development of this research.

Author contributions

Sergio Gomez: conceptualization, data curation, investigation, writing–original draft; Joszaira Lárez: supervision, data validation.

Conflict of interest

The authors declare no conflict of interest.

References

1. Ahmad W, McCormack SJ, Byrne A (2025) Biocomposites for sustainable construction: A review of material properties, applications, research gaps, and contribution to circular economy. *J Build Eng* 105: 112525. https://doi.org/10.1016/j.jobe.2025.112525
2. Vishwash B, Shivakumar ND, Sachidananda KB (2025) A brief review on natural fiber reinforced composite sandwich structures. *Next Res* 2: 100474. https://doi.org/10.1016/j.nexres.2025.100474
3. Mulenga TK, Rangappa SM, Siengchin S (2025) Impact behavior of natural fiber composites: A comprehensive review on theoretical and computational modeling. *Next Mater* 8: 100849. https://doi.org/10.1016/j.nxmate.2025.100849
4. Ajayi NE, Rusnakova S, Ajayi AE, et al. (2025) A comprehensive review of natural fiber reinforced polymer composites as emerging materials for sustainable applications. *Appl Mater Today* 43: 102666. https://doi.org/10.1016/j.apmt.2025.102666
5. Wadgave I, Kulkarni S, Katekar S, et al. (2024) A comprehensive review on: Mechanical and acoustical characterization of natural fiber-reinforced composite. *Mater Today Proc*. https://doi.org/10.1016/j.matpr.2024.05.002
6. Mohammed M, Oleiwi JK, Mohammed AM, et al. (2024) A review on the advancement of renewable natural fiber hybrid composites: prospects, challenges, and industrial applications. *J Renew Mater* 12: 1237–1290. https://doi.org/10.32604/jrm.2024.051201
7. Muñoz-Blandón O, Ramírez-Carmona M, Rendón-Castrillón L, et al. (2023) Exploring the potential of fique fiber as a natural composite material: A comprehensive characterization study. *Polymers* 15: 2712. https://doi.org/10.3390/polym15122712
8. Rendón-Castrillón L, Ramírez-Carmona M, Ocampo-López C, et al. (2022) The industrial potential of fique cultivated in Colombia. *Sustainability* 15: 695. https://doi.org/10.3390/su15010695
9. Laverde Sarmiento V, Benjumea JM, Rincón Ortiz M (2025) Chemical and mechanical characterization of treated and untreated woven fique fiber textiles as an alternative external reinforcement for concrete. *J Nat Fibers* 22: 2462975. https://doi.org/10.1080/15440478.2025.2462975
10. Pabón Rojas JJ, Ramón Valencia BA, Bolívar Osorio FJ, et al. (2021) The role of fiber-matrix compatibility in vacuum processed natural fiber/epoxy biocomposites. *Cellulose* 28: 7845–7857. https://doi.org/10.1007/s10570-021-04055-7

11. Rua J, Buchely MF, Monteiro SN, et al. (2021) Impact behavior of laminated composites built with fique fibers and epoxy resin: A mechanical analysis using impact and flexural behavior. *J Mater Res Technol* 14: 428–438. https://doi.org/10.1016/j.jmrt.2021.06.068
12. Gómez-Suarez SA, Córdoba-Tuta E (2022) Composite materials reinforced with fique fibers—A review. *Rev UIS Ing* 21: 163–178. https://doi.org/10.18273/revuin.v21n1-2022013
13. Barros FA, Gamboa JM, Díaz-Ramírez GA, et al. (2019) Numerical and experimental study of flexural behaviour in polymer composite materials reinforced with natural fique textiles. *J Phys Conf Ser* 1247: 012001. https://doi.org/10.1088/1742-6596/1247/1/012001
14. González-Estrada OA, Díaz-Ramírez G, Quiroga Mendez JE (2018) Mechanical response and damage of woven composite materials reinforced with fique. *Key Eng Mater* 774: 143–148. https://doi.org/10.4028/www.scientific.net/KEM.774.143
15. Chaves Garcia MC, Castro Bermudez JD, Pertuz Comas AD (2024) Uniaxial fatigue study of a natural-based bio-composite material reinforced with fique natural fibers. *Frat Ed Integrità Strutt* 18: 94–108. https://doi.org/10.3221/IGF-ESIS.68.06
16. Avila De Cêa BS, Pereira Junio RF, Silva DS, et al. (2025) An experimental and numerical study of the ballistic behavior of an epoxy matrix hybrid composite reinforced with aramid fabric and fique fabric. *J Mater Res Technol* 35: 2037–2054. https://doi.org/10.1016/j.jmrt.2025.01.172
17. Castro D, Pertuz A, León-Becerra J (2022) Mechanical behavior analysis of a vertical axis wind turbine blade made with fique-epoxy composite using FEM. *Procedia Comput Sci* 203: 310–317. https://doi.org/10.1016/j.procs.2022.07.039
18. Gómez S, Ramón B, Guzmán R (2018) Análisis modal de material compuesto de resina bioepoxy/fibra de fique. *Entre Cienc E Ing* 12: 78–83. https://doi.org/10.31908/19098367.3706
19. Gómez SA, Córdoba E, Vega Mesa C, et al. (2021) Manufacture of student chair in composite material reinforced with fique fiber. *Sci Tech* 26: 6–13. https://doi.org/10.22517/23447214.24509
20. Wang W, Wang H, Fei S, et al. (2022) Concurrent multiscale modeling of in-plane micro-damage evaluation in Z-pinned composite laminates. *Compos Struct* 295: 115842. https://doi.org/10.1016/j.compstruct.2022.115842
21. Hou Y, Wang W, Meng L, et al. (2022) An insight into the mechanical behavior of adhesively bonded plain-woven-composite joints using multiscale modeling. *Int J Mech Sci* 219: 107063. https://doi.org/10.1016/j.ijmecsci.2022.107063
22. Zhang M, Yu Y, Li L, et al. (2024) A molecular dynamics assisted insight on damping enhancement in carbon fiber reinforced polymer composites with oriented multilayer graphene oxide coatings. *Microstructures* 4: 2024051. https://doi.org/10.20517/microstructures.2024.29
23. Shu W, Stanciulescu I (2020) Multiscale homogenization method for the prediction of elastic properties of fiber-reinforced composites. *Int J Solids Struct* 203: 249–263. https://doi.org/10.1016/j.ijsolstr.2020.08.009
24. Fedorenko A, Zhao C, Liu H, et al. (2026) Damage-rate-dependent model for impact crushing of thin-ply CFRP tubes. *Int J Mech Sci* 313: 111268. https://doi.org/10.1016/j.ijmecsci.2026.111268
25. Govilas J, Chevallier A, Akleh W, et al. (2024) Mechanical behavior and apparent stiffness of flax, hemp and nettle fibers under single fiber transverse compression tests. *Compos Part A* 185: 108321. https://doi.org/10.1016/j.compositesa.2024.108321
26. Piggott MR (1980) Failure processes, In: Piggott MR, *Load-Bearing Fibre Composites*, Oxford: Pergamon, 100–125. https://doi.org/10.1016/B978-0-08-024231-6.50011-8

27. Callister WD, Rethwisch DG (2020) *Materials Science and Engineering: An Introduction: SI Version*, 10th Eds., Hoboken, NJ: Wiley.
28. Wang Y, Huang Z (2017) A review of analytical micromechanics models on composite elastoplastic behaviour. *Procedia Eng* 173: 1283–1290. https://doi.org/10.1016/j.proeng.2016.12.159
29. Raju B, Hiremath SR, Roy Mahapatra D (2018) A review of micromechanics based models for effective elastic properties of reinforced polymer matrix composites. *Compos Struct* 204: 607–619. https://doi.org/10.1016/j.compstruct.2018.07.125
30. Habbar G, Maizia A, Hocine A, et al. (2022) Micromechanical analysis of a bio-sandwich application for cylinder under pressure. *J Compos Sci* 6: 69. https://doi.org/10.3390/jcs6030069
31. Yan W, Shi S, Xiao L, et al. (2024) The influence of the interface on the micromechanical behavior of unidirectional fiber-reinforced ceramic matrix composites: An analysis based on the periodic symmetric boundary conditions. *Symmetry* 16: 695. https://doi.org/10.3390/sym16060695
32. Jones RM (1999) *Mechanics of Composite Materials*, 2nd Eds., Boca Raton: CRC Press. https://doi.org/10.1201/9781498711067
33. Lakshmi Narayana V, Bhaskara Rao L (2021) A brief review on the effect of alkali treatment on mechanical properties of various natural fiber reinforced polymer composites. *Mater Today Proc* 44: 1988–1994. https://doi.org/10.1016/j.matpr.2020.12.117
34. Shelly D, Singhal V, Jaidka S, et al. (2025) Mechanical performance of bio-based fiber reinforced polymer composites: A review. *Polym Compos* 46: 9–43. https://doi.org/10.1002/pc.30000
35. Mehdikhani M, Gorbatikh L, Verpoest I, et al. (2019) Voids in fiber-reinforced polymer composites: A review on their formation, characteristics, and effects on mechanical performance. *J Compos Mater* 53: 1579–1669. https://doi.org/10.1177/0021998318772152
36. Rodríguez LJ, Sarache WA, Orrego CE (2014) Compuestos de poliéster reforzados con fibra de plátano/banano (Musa paradisiaca) modificada químicamente: comparación con fibra de vidrio y fique (Furcraea andina). *Inf Tecnol* 25: 27–34. https://doi.org/10.4067/S0718-07642014000500005
37. Ng WK, Johar M, Israr HA, et al. (2020) A review on the interfacial characteristics of natural fibre reinforced polymer composites, In: Goh KL, MK A, Silva RTD, et al., *Interfaces in Particle and Fibre Reinforced Composites,* Cambridge: Woodhead Publishing, 163–198. https://doi.org/10.1016/B978-0-08-102665-6.00007-8
38. Zhou D, Tong X, Liu H, et al. (2024) A modified Halpin–Tsai model for predicting the elastic modulus of composite materials. *AIP Adv* 14: 015157. https://doi.org/10.1063/5.0160256
39. Yang L, Gao J, Zhang R, et al. (2026) Microscale modeling and damage mechanisms of fiber-reinforced composites with perpendicularly embedded optical fibers. *Polym Compos* 47: 6550–6560. https://doi.org/10.1002/pc.70573
40. Ramam R, Padal KT (2022) Effect of fiber orientation on the mechanical properties of natural fiber epoxy reinforced composites of flax, hemp, and kenaf. *Int J Adv Technol Eng Explor* 9: 72–81. https://doi.org/10.19101/IJATEE.2021.874747
41. Hossain MS, Anwar MS, Islam MS, et al. (2024) Effect of fiber orientation and volume fraction on Young's modulus for unidirectional carbon fiber reinforced composites: A numerical investigation. *Malays J Compos Sci Manuf* 13: 45–54. https://doi.org/10.37934/mjcsm.13.1.4554

42. Memarzadeh A, Onyibo EC, Asmael M, et al. (2024) Dynamic effect of ply angle and fiber orientation on composite plates. *Spectr Mech Eng Oper Res* 1: 90–110. https://doi.org/10.31181/smeor11202410
43. Rajpurohit SR, Dave HK, Bodaghi M (2024) Classical laminate theory for flexural strength prediction of FDM 3D printed PLAs. *Mater Today Proc* 101: 51–58. https://doi.org/10.1016/j.matpr.2023.03.310
44. Castilho E, Firmo JP, Garrido M, et al. (2025) Application of classical laminate theory to predict the effect of elevated temperature on the elastic modulus of GFRP composites. *Constr Build Mater* 494: 143445. https://doi.org/10.1016/j.conbuildmat.2025.143445
45. Mulenga TK, Ude AU, Vivekanandhan C (2021) Techniques for modelling and optimizing the mechanical properties of natural fiber composites: A review. *Fibers* 9: 6. https://doi.org/10.3390/fib9010006

AIMS Press